J. Fluid Mech. (2004), *vol.* 498, *pp.* 73–111.
DOI: 10.1017/S0022112003006529 Printed in the United Kingdom

On spray formation

By P. MARMOTTANT† AND E. VILLERMAUX‡

IRPHE, Université de Provence, Aix–Marseille 1, Technopôle de Château-Gombert, 49, rue Frédéric Joliot-Curie, 13384 Marseille Cedex 13, France

(Received 4 November 2002 and in revised form 25 July 2003)

We depict and analyse the successive steps of atomization of a liquid jet when a fast gas stream blows parallel to its surface. Experiments performed with various liquids in a fast air flow show that the liquid destabilization proceeds from a two-stage mechanism: a shear instability first forms waves on the liquid. The transient acceleration experienced by the liquid suggests that a Rayleigh–Taylor type of instability is triggered at the wave crests, producing liquid ligaments which further stretch in the air stream and break into droplets. The primary wavelength $\lambda \sim \delta(\rho_1/\rho_2)^{1/2}$ is set by the vorticity thickness δ, in the fast air stream and the liquid/gas density ratio ρ_1/ρ_2. The transverse corrugations of the crests have a size $\lambda_\perp \sim \delta We_\delta{}^{-1/3}(\rho_1/\rho_2)^{1/3}$, where $We_\delta = \rho_2 u_2^2 \delta/\sigma$ is the Weber number constructed on the gas velocity u_2 and liquid surface tension σ. The ligament dynamics gives rise, after break-up, to a well-defined droplet size distribution whose mean is given by $\lambda_\perp$. This distribution bears an exponential tail characteristic of the broad size statistics in airblast sprays.

1. Introduction

The disintegration and dispersion of a liquid volume by a gas stream is a phenomenon which embraces many natural and industrial operations. The entrainment of spume droplets by the wind over the ocean, the generation of pharmaceutical sprays or the atomization of liquid propellants in combustion engines are among obvious examples (Lefebvre 1989; Bayvel & Orzechowski 1993). In order to compute the rate of exchanges of solutes between the ocean and the atmosphere, or to estimate the size of a combustion chamber, it is frequently desirable to have a precise knowledge of the liquid dispersion structure, in particular its distribution of droplet sizes as a function of the external parameters: wind speed, liquid surface tension, etc.

The problem has first been investigated in the simple configuration of a single drop immersed in a flow moving relatively to itself (Hinze 1949; Kolmogorov 1949; Lane 1951). It was realized that the relevant parameter for the drop breakup criterion is the Weber number (Weber 1931), constructed as the ratio of the drag, aerodynamic pressure $\rho_2(u_2-u_1)^2$ and the capillary restoring pressure σ/d as $We = \rho_2(u_2-u_1)^2 d/\sigma$, where ρ_2 denotes the density of the destabilizing flow, $u_2 - u_1$ the contrast of velocity between the flow and the droplet, d its diameter and σ the liquid surface tension. The critical Weber number above which the droplet disintegrates is about 10 (Hanson, Domich & Adams 1963) and somewhat smaller when the destabilizing flow is turbulent (Hinze 1955).

† Present address: Department of Applied Physics, WB Building, University of Twente, 7500 AE Enschede, The Netherlands.

‡ Also at: Institut Universitaire de France.

The detailed breakup mechanism reveals a very rich zoology of phenomena (Pilch & Erdman 1987). At moderate Weber number, the droplet deforms in a pancake shape which flattens in a bag membrane eventually breaking into very small droplets (originating from the membrane itself) and larger droplets (coming from the membrane rim).

At higher Weber numbers, the droplet is no longer deformed as a whole, but is rather 'stripped' at its surface, forming liquid fibres, or ligaments which produce the stable droplets (Ranger & Nicholls 1969; Krzeczkowski 1980; Joseph, Belanger & Beavers 1999).

The same qualitative succession of atomization regimes is observed when a liquid jet flows in a faster coaxial stream (Faragó & Chigier 1992; Zaleski *et al.* 1996), except that there is no critical Weber number for the jet disintegration since its circular geometry suffers a capillary-driven instability (Plateau 1873; Rayleigh 1879). However, the effect of the air on the liquid destabilization is manifested, as shown on figure 1, first as a global wandering of the jet inducing bags and rims, then as the air velocity is increased, via the formation of ligaments at a scale smaller than the liquid jet diameter itself. In this 'stripping' regime, the typical droplet diameter (often characterized by the mean Sauter diameter d_{32} representing the third over the second moment of the size distribution $P(d)$) has been found to depend on the velocity contrast like $(u_2 - u_1)^{-\beta}$, with β close to 1 (Yatsuyanagi, Sakamoto & Sato 1994; Lasheras, Villermaux & Hopfinger 1998 and references therein). The problem is, obviously, Galilean invariant and the same 'stripping' phenomenology occurs when a liquid jet is moving in a still atmosphere, as can be seen from the early instantaneous pictures of Hoyt & Taylor (1977). The droplet size was also found to decrease with the velocity contrast, given by, in that case, the liquid velocity (Wu & Faeth 1995).

A salient feature of natural sprays is the broadness of their droplet size distribution; the distribution is highly skewed, the most probable droplet sizes being close to the smallest ones and the probability of finding a drop size twice or three times larger than the mean being not vanishingly small (Simmons 1977*a*, *b*; Anguelova & Barber 1999; Andreas, Pattison & Belcher 2001). Simmons (1997*a*, *b*) notes that, for a large collection of industrial sprays, the distribution of sizes $P(d)$ is, in shape, solely determined by its mean, and that its tail is well fitted by an exponential fall-off. The existing theories intended to model this fragmentation process essentially rely on cascade ideas, following the early suggestion of Kolmogorov (1949) (see also Novikov & Dommermuth 1997), leading to log-normal statistics of the fragment sizes. Notable exceptions are the work of Longuet-Higgins (1992) which shows how a simple geometrical model of ligament random break-up produces broad skewed size distribution without resorting to sequential cascade arguments, and that of cohen (1990, 1991) which shows how pure combinatoric and thermodynamic arguments lead to a Poisson distribution for the fragment volumes.

As suggested by figure 1, at the root of the disintegration process is a shear between the light fast stream and the slow dense liquid. Adapting an analysis of Rayleigh (1880), Villermaux (1993, 1998*a*) has shown why and how, when the velocity profile at the liquid–gas interface is not a pure discontinuity, the instability Kelvin and Helmholtz analysis has to be altered to predict the most amplified wavelength and growth rate. Using a plane liquid–gas shear layer, Raynal (1997) and Raynal *et al.* (1997) have shown experimentally that the presence of a smooth cross-over between the slow and the fast velocity is indeed a key ingredient to understanding the first destabilization of the liquid.

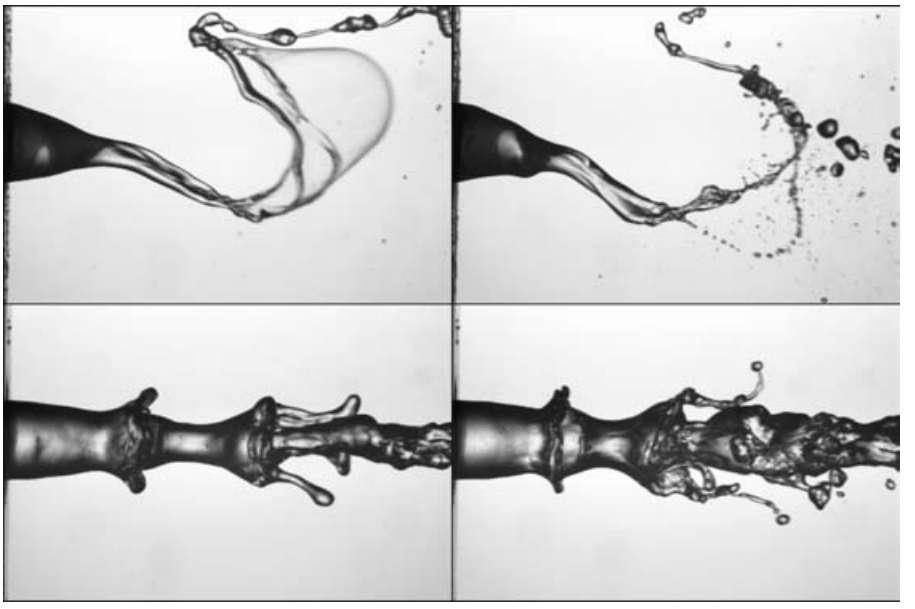

FIGURE 1. Breakup regimes of a slow dense liquid jet by a fast light coaxial stream. Top: at low gas velocity, the liquid jet meanders in the gas stream, possibly forming bags. Bottom: for higher gas velocities, the jet is peeled-off at its surface, disintegrating via a succession of surface instabilities.

The present paper reports a comprehensive study of the atomization scenario, from the primary destabilization of the liquid–gas interface, to the final drop size distribution. Section 2 presents the experimental set-up, § 3 gives a general overview of the chronology of the mechanisms and presents results, § 4 is devoted to the analysis of the interface destabilization, and § 5 discusses the drop formation statistics. The – practically important – effect of a pre-existing turbulence in the gas, or the liquid, or both is examined in the Appendices.

2. Experimental set-up

The flow configuration was designed to realize a round liquid jet surrounded by a tangential (coaxial) air flow (figure 2). The choice of the axisymmetric geometry was made for visualization purposes. It has, also, a direct relevance for practical questions regarding liquid–gas propellant engines.

The convergence of the flow in the injector reduces the intensity of pre-existent turbulence. The contraction of the cross-section is of a factor 6.9 for the liquid jet and 6 for the gas jet. The liquid flow velocity is measured by a rotameter (manufacturer Kobold) with an accuracy of 2%, and the air velocity by a turbine flowmeter (McMillan) with an accuracy of 3%. The liquids were: tap water; ethanol 95%; and a solution of glycerol in water (66% in mass) whose properties are given in table 1.

The air (pressurized up to 6 bars at the inlet) flows through the outer chamber, and a boundary layer develops on the wall of the injector. The velocity profiles at the exit, we obtained by standard hot-wire anemometry (figure 3*a*).

The boundary-layer thickness in the gas is defined by the vorticity thickness δ

$$\delta = \frac{U_{max} - U_{min}}{\mathrm{d}U/\mathrm{d}y|_{max}} \tag{2.1}$$

	Surface tension ($mN\,m^{-1}$)	Density	Viscosity (centiPoise)
Water	69 ± 1	1	1.14 ± 0.01
Ethanol	25 ± 1	0.79	1.34
Glycerol 66%	70 ± 1	1.16	14.0 ± 0.2

TABLE 1. Liquid properties measured at 20°C.

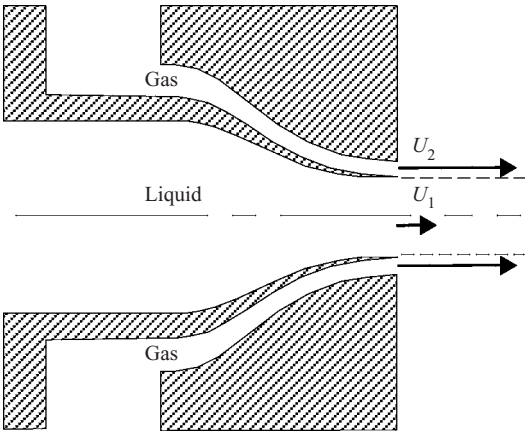

FIGURE 2. Injector geometry: the inner diameter is $D_1 = 7.8$ mm, the annulus gap has a width of $h = 1.7$ mm.

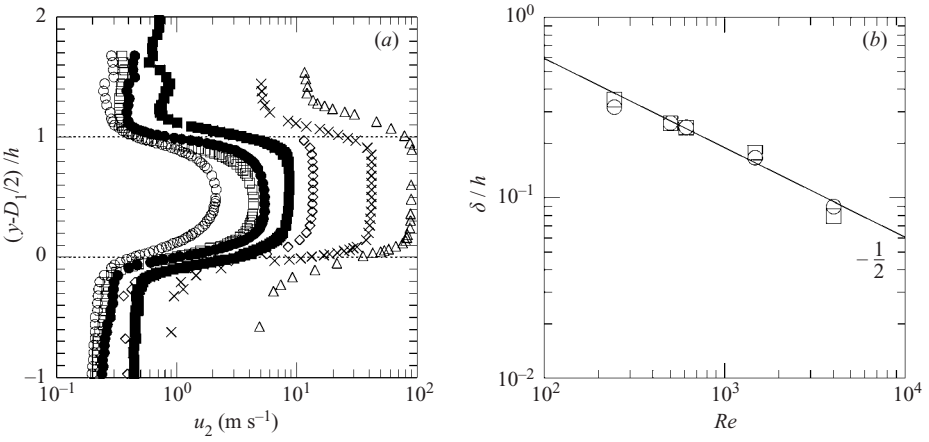

FIGURE 3. (*a*) Velocity profiles on a radius through the outer air jet. Maximal air velocities of 2.1, 4.3, 5.4, 8.7, 14, 42 and 90 m s^{-1}. (*b*) Vorticity thickness as a function of $Re = hu_{\max}/\nu_2$: ○, boundary layer on the splitting plate; □, outer wall; —, $5.6Re^{-1/2}$.

and decreases with air velocity. Expressed as a function of the Reynolds number based on the gas gap thickness h of the crown at exit, $Re = hu_2/\nu_2$, it varies according to

$$\delta/h \simeq 5.6\,Re^{-1/2}, \tag{2.2}$$

as expected for a laminar boundary layer (figure 3*b*). As will be emphasized below, this quantity is a key parameter controlling the instabilities at the liquid surface.

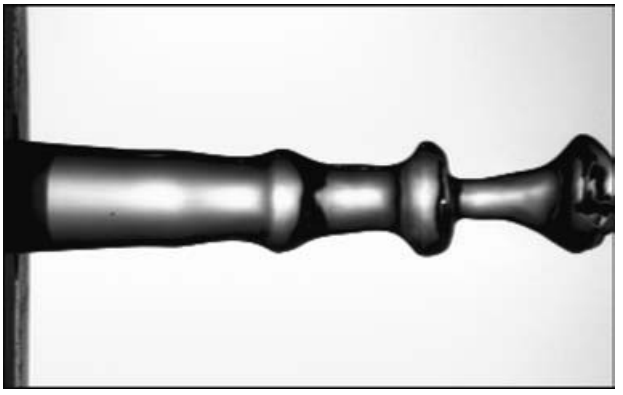

FIGURE 4. Growth of axisymmetric instability ($u_1 = 0.5\,\mathrm{m\,s^{-1}}$, $u_2 = 15\,\mathrm{m\,s^{-1}}$).

The liquid jet was made visible by backward illumination through a diffusive screen. Two imaging techniques were used. For length and displacement measurements, a high-resolution camera (Orca, Hamamatsu, 1284×1024 pixels) was mounted in combination with a couple of 5 μs xenon flash lamps (FXP 850, EG&G ElectroOptics). To follow the entire evolution of the motion, a high-speed camera (Hs Motion Analyser, Kodak, up to 4500 images per second with full resolution 256×256 pixels) is combined with a continuous 1000 W halogen spot. The resulting digital images were analysed with the NIH Image freeware. Droplet size statistics typically involved 2000 objects.

3. Disintegration chronology, and results

When emerging in a still atmosphere (gas velocity $u_2 = 0$), the liquid jet (velocity u_1) suffers a capillary Plateau–Rayleigh instability. Axisymmetric undulations grow along the jet with a wavelength $4.51 D_1$ at onset, eventually breaking the jet in droplets.

Adding a coflowing stream of air with velocity u_2, large in comparison to u_1, induces a new axisymmetric destabilization of the liquid jet, which eventually overcomes the Plateau–Rayleigh instability, when u_2 is increased.

3.1. *Axisymmetric instability*

The wavelength of the liquid jet undulations in the presence of air flow are measured on still pictures (figure 4). This wavelength is clearly distinct from that due to the capillary instability since it is a function of the air velocity. It is not, either, due to a pulsation of the axial liquid velocity which would actually lead to similar undulations (Meier, Klöpper & Grabitz 1992). At $u_2 = 15\,\mathrm{m\,s^{-1}}$ the wavelength is of the order of D_1 and decreases with larger air velocity proportionally to the vorticity thickness δ (figure 5*a*). The liquid velocity affects the wavelength slightly; larger wavelengths are obtained with smaller u_1.

The passage frequencies of the undulations were measured aiming a laser round beam perpendicular to the jet axis such that the beam (about 2 mm in diameter) intersects the liquid surface at a fixed downstream position (typically one liquid diameter). The beam impacts on a photodiode and is deflected by the passage of an undulation, resulting in a modulation of the signal received by the photodiode. The temporal spectrum of the photodiode signal displays a peak at the mean undulations passage frequency. This frequency increases rapidly with air velocity, like $u_2^{3/2}$ (figure 5*b*).

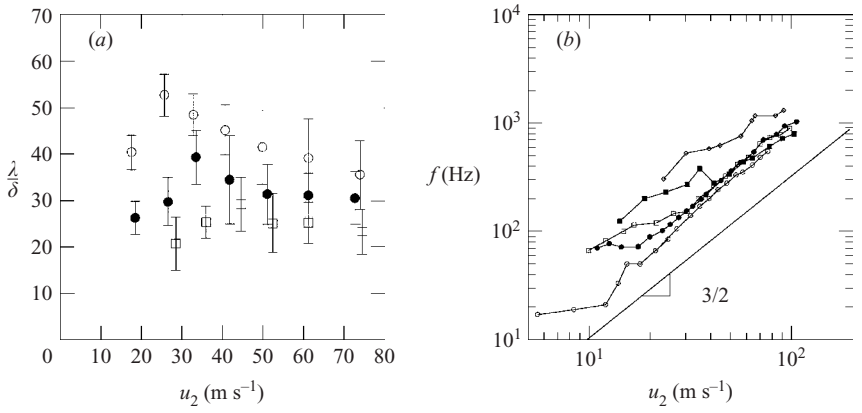

FIGURE 5. (*a*) Ratio of the wavelength of the initial instability to the thickness of the air boundary layer as a function of the air Reynolds number $Re = hu_2/\nu_2$ (○ , $u_1 = 0.45\,\mathrm{m\,s^{-1}}$, ●, $0.94\,\mathrm{m\,s^{-1}}$, □, $2\,\mathrm{m\,s^{-1}}$). (*b*) Frequency of occurrence of the undulations; ○, $u_1 = 0.20\,\mathrm{m\,s^{-1}}$; ●, $0.32\,\mathrm{m\,s^{-1}}$; □, $0.45\,\mathrm{m\,s^{-1}}$; ■, $0.80\,\mathrm{m\,s^{-1}}$; ◇, $1.69\,\mathrm{m\,s^{-1}}$.

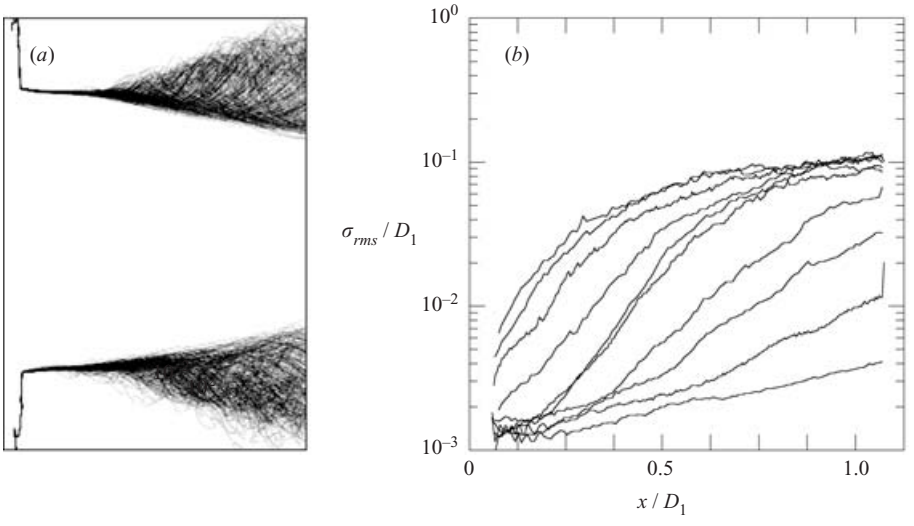

FIGURE 6. (*a*) Superposition of the liquid contours ($u_1 = 1\,\mathrm{m\,s^{-1}}$, $u_2 = 33\,\mathrm{m\,s^{-1}}$). (*b*) Deviation of the jet radius as a function of the downstream distance x. From bottom to top, air velocities are 18, 21, 25, 27, 29, 30, 33, 38, 48 and $57\,\mathrm{m\,s^{-1}}$, $u_1 = 0.94\,\mathrm{m\,s^{-1}}$.

The downstream growth of the undulations is measured by superimposing a large collection of instantaneous contours of the liquid surface (figure 6*a*). The undulations amplitude is estimated by the r.m.s. deviation of the jet radius at a fixed downstream position $\sigma_{\mathrm{rms}} = \langle (r_i - \langle r_i \rangle)^2 \rangle^{1/2}$, $\langle . \rangle$ being an ensemble average over many instantaneous pictures. If the jet oscillations were perfectly sinusoidal with an amplitude $a(x)$, their r.m.s. deviation would be $\sigma_{\mathrm{rms}} = a/\sqrt{2}$. The amplitude of the observed oscillations display an initial exponential growth which saturates when the amplitude approaches 5% of the liquid jet diameter D_1 (figure 6*b*).

3.2. *Transverse instability: the birth of digitations*

Above a critical velocity (of about $20\,\mathrm{m\,s^{-1}}$), the undulations are no longer axisymmetric and display transverse azimuthal modulations. These modulations grow in

FIGURE 7. Development of digitations ($u_1 = 0.6\,\mathrm{m\,s^{-1}}$, $u_2 = 35\,\mathrm{m\,s^{-1}}$).

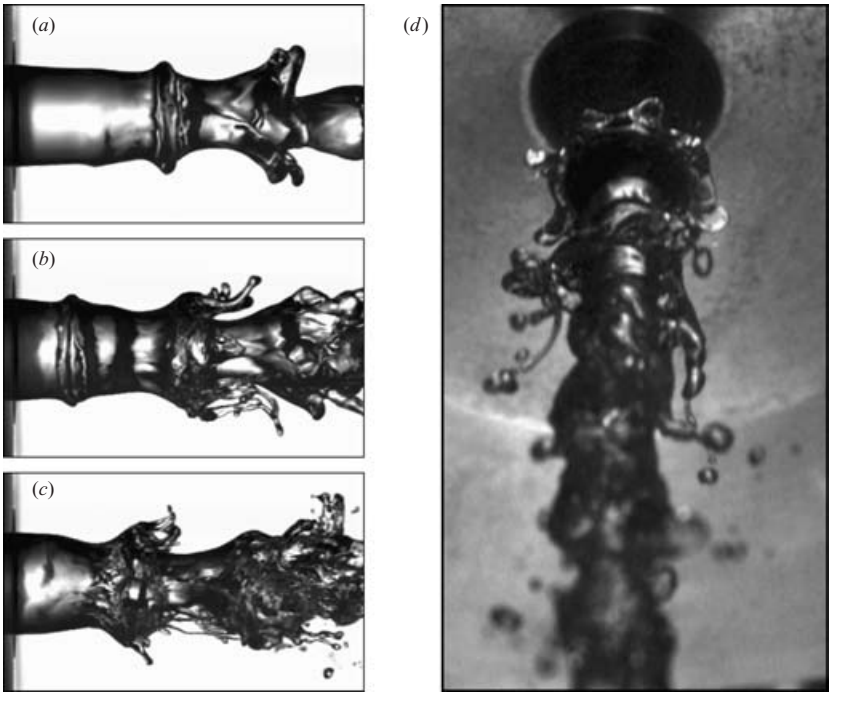

FIGURE 8. Transverse modulation, (*a*) $u_2 = 24\,\mathrm{m\,s^{-1}}$; (*b*) $u_2 = 27\,\mathrm{m\,s^{-1}}$; (*c*) $u_2 = 32\,\mathrm{m\,s^{-1}}$; (*d*) $u_2 = 24\,\mathrm{m\,s^{-1}}$ in oblique view.

amplitude and eventually degenerate in liquid ligaments which are further accelerated in the fast air stream (figures 7 and 8).

Photographs taken from the side allow us to estimate the number n of liquid ligaments at the crest of the primary undulations. Their number increases with air

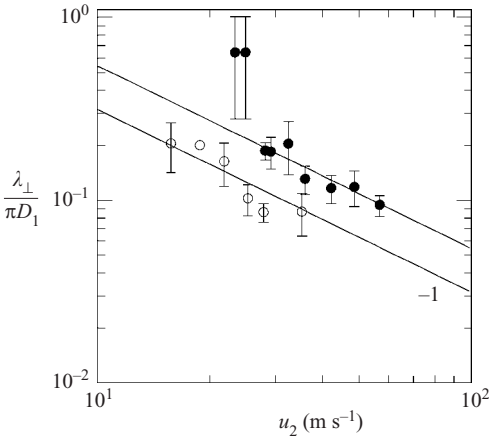

FIGURE 9. Average transverse spacing of the digitations; ●, water; ○, ethanol; $u_1 = 0.94\,\mathrm{m\,s^{-1}}$.

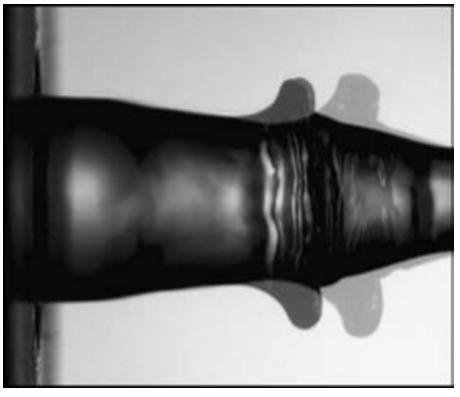

FIGURE 10. Double flashes on one exposure. $u_1 = 0.45\,\mathrm{m\,s^{-1}}$, $u_2 = 19\,\mathrm{m\,s^{-1}}$, $\Delta t = 2$ ms.

velocity. The ligaments are fairly equally distributed around the liquid jet and their mean spacing $\lambda_\perp = \pi D_1/n$ decreases approximately as u_2^{-1} (figure 9). Surface tension plays a role in setting the absolute value of this spacing; with ethanol, whose surface tension is smaller than that of water, the spacing is smaller. The jets made of a mixture of water and glycerol (66% by weight, 14 times more viscous than pure water) do not present an appreciably different spacing from that of water for a given air velocity.

3.3. *Ligament development*

After the onset of the primary, shear instability causing the axisymmetric disturbances, the acceleration of the liquid surface protrusions by the air presents two stages. First, the crest of the primary transverse modulations are displaced as a whole relative to the liquid bulk and, secondly, the azimuthal modulations are elongated into ligaments.

3.3.1. *Acceleration of the modulations*

The acceleration of the crests is estimated by their displacement on double exposure pictures (figure 10). The delay Δt between the exposures is adjustable and is of the order of a millisecond. This method allows us to use a high-resolution camera with a slow framing rate providing high-precision measurements. The velocity between the

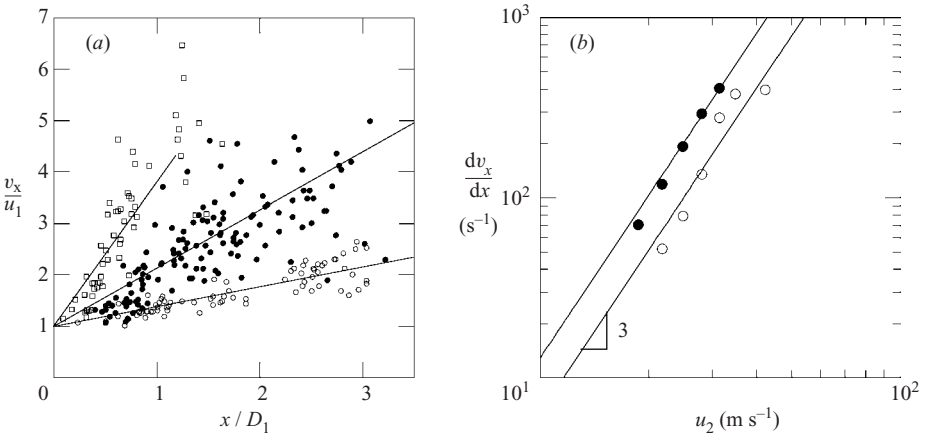

FIGURE 11. (*a*) Axial velocity of the crest as recorded on double flash photographs, $u_1 = 0.94\,\mathrm{m\,s^{-1}}$. ○, $u_2 = 21\,\mathrm{m\,s^{-1}}$; ●, $u_2 = 28\,\mathrm{m\,s^{-1}}$; □, $u_2 = 34\,\mathrm{m\,s^{-1}}$. —, linear trend. (*b*) Variation of the velocity of the crest, according to slopes of the previous graph; ●, $u_1 = 0.45\,\mathrm{m\,s^{-1}}$; ○, $u_1 = 0.94\,\mathrm{m\,s^{-1}}$.

two positions of the crest x_1 and x_2 is defined as $v_x = (x_2 - x_1)/\Delta t$ and is plotted as a function of downstream distance x_1 on figure 11(*a*).

The velocity of the liquid is initially that of the liquid u_1 since the surface is smooth and not yet perturbed by any instability waves. When the amplitude of undulations is high enough, aerodynamic drag comes into play and the liquid is accelerated. The velocities have a large dispersion from crest to crest, but an initial linear growth with the downstream distance is nevertheless easily noticeable. The spatial increase of velocity, $\mathrm{d}v_x/\mathrm{d}x$, is proportional to ${u_2}^3$ and inversely proportional to u_1 (figure 11*b*).

3.3.2. *Elongation of the modulations*

The dynamics of the ligaments coming from the azimuthal destabilization of the wave crest is followed using high-speed imaging. The temporal evolution of the length L is shown on figure 12(*a*).

A selection of representative ligaments for different air velocities shows (figure 12*b*) that the rate of stretch and the thickness of the ligaments at breakup depend strongly on the air velocity.

3.4. *Ligament breakup*

The liquid ligaments are stretched in the air stream and their diameter decreases until they break into drops (figure 13).

The ligament length L_b and diameter ξ_b just before breakup can be measured on double exposed high-resolution photographs, when the breakup occurs between the two flashes. The evolution of these lengthscales with the gas velocity u_2 is shown on figure 14; at breakup, the ligament length does not vary much, while the diameter strongly decreases with u_2 (figure 15).

The liquid volume contained in one ligament is found by adding the volume of all the droplets resulting from the ligament breakup. The identification of the droplets produced by the same ligament is performed on the two exposure photographs. The volume of each droplet is measured from its surface S on the image, assuming that it is close to a sphere of diameter d, such that $S = \pi d^2/4$. The total volume of the ligament, difficult to follow during its elongation, is in that way accurately measured

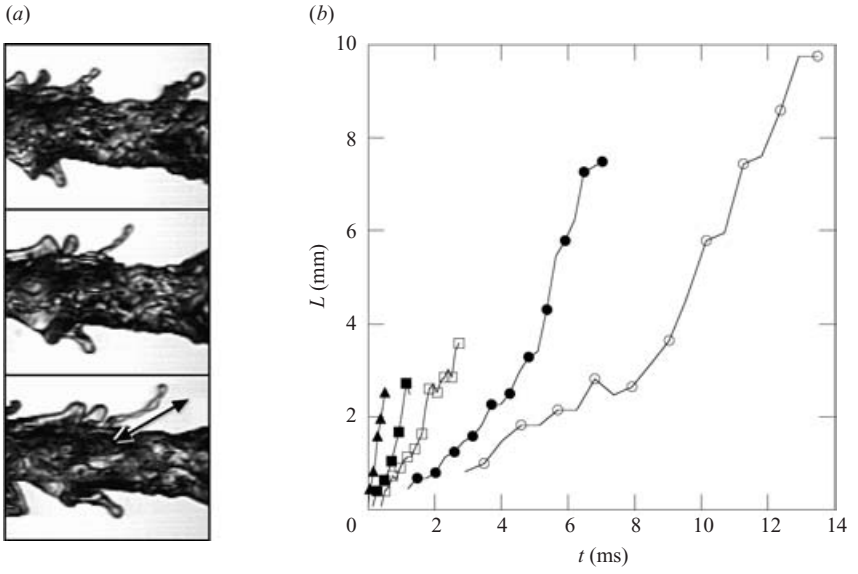

FIGURE 12. (*a*) Ligament elongation ($\Delta t = 1$ ms, $u_1 = 1\,\mathrm{m\,s^{-1}}$, $u_2 = 25\,\mathrm{m\,s^{-1}}$). (*b*) Length of the ligaments with time. The end of the curve corresponds to their breakup. ○, $u_2 = 25\,\mathrm{m\,s^{-1}}$; ●, $u_2 = 29\,\mathrm{m\,s^{-1}}$; □, $u_2 = 34\,\mathrm{m\,s^{-1}}$; ■, $u_2 = 40\,\mathrm{m\,s^{-1}}$; ▲, $u_2 = 50\,\mathrm{m\,s^{-1}}$.

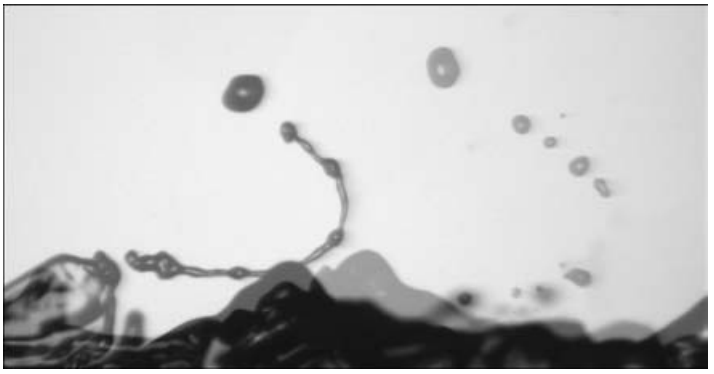

FIGURE 13. Breakup of a ligament.

as the sum of the droplet volumes, $v_0 = \sum_i \pi d_i^3/6$. In what follows, we express the total ligament volume by the size d_0 which is the diameter of the equivalent sphere containing all the ligament volume

$$v_0 = \tfrac{1}{6}\pi {d_0}^3. \tag{3.1}$$

The average (among a set of ligaments obtained for given operating conditions) ligament 'size' $\langle d_0 \rangle$ defined that way is found to decrease with the air velocity like u_2^{-1}, thus following an evolution parallel to that of $\lambda_\perp$

$$\langle d_0 \rangle \simeq 0.23 \lambda_\perp, \tag{3.2}$$

as figures 9 and 15 show, where 0.23 is the observed prefactor.

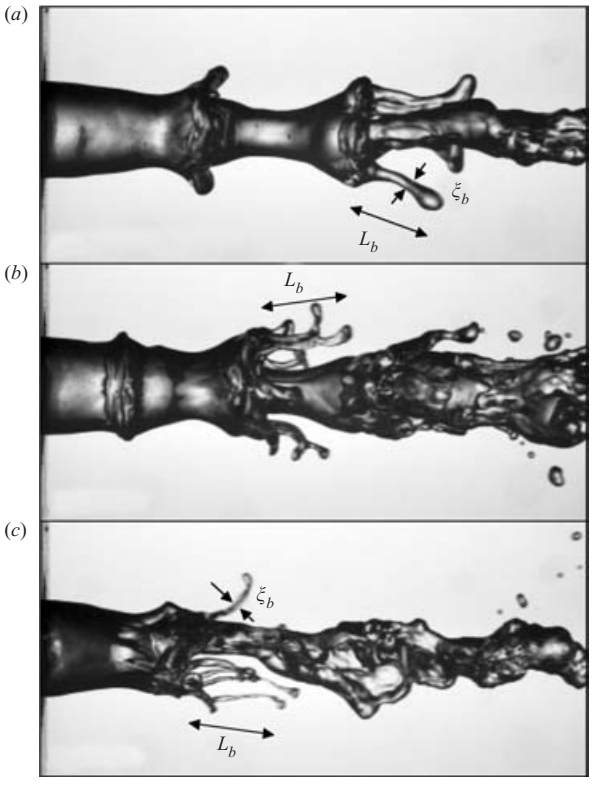

FIGURE 14. Aspect of ligaments before breakup. (*a*) $u_2 \sim 20\,\mathrm{m\,s^{-1}}$; (*b*) $35\,\mathrm{m\,s^{-1}}$; (*c*) $50\,\mathrm{m\,s^{-1}}$.

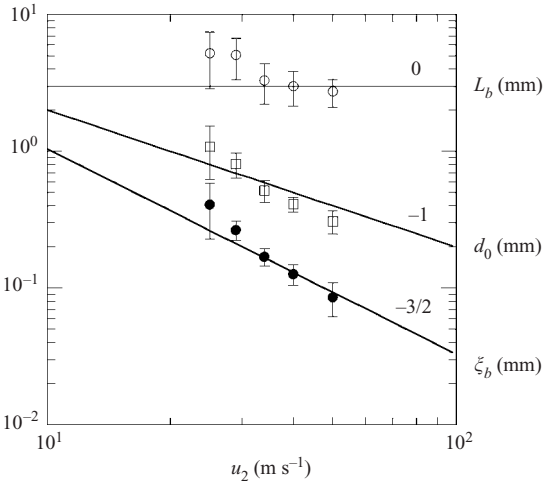

FIGURE 15. Evolution of length L_b and diameter ξ_b of the ligaments before breakup, along with their volume expressed by their size d_0 (water).

3.5. *Droplet sizes from one ligament*

For given operating conditions, the ligament sizes d_0 are found to be distributed around the mean in a somewhat symmetric bell-shaped distribution (figure 16*a*).

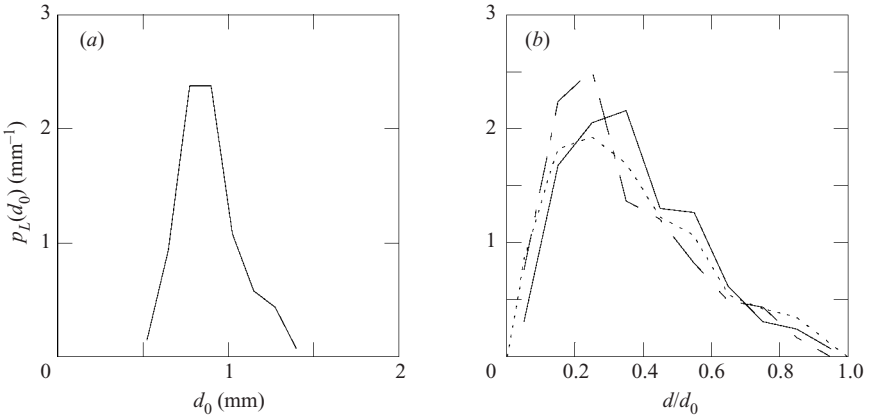

FIGURE 16. (*a*) Probability density function of the ligaments size $p_L(d_0)$, for the same flow condition. 111 measurements distributed in 8 bins, $u_1 = 0.45\,\mathrm{m\,s^{-1}}$, $u_2 = 29\,\mathrm{m\,s^{-1}}$. (*b*) Distribution $p_B(d/d_0)$ of the droplet sizes after breakup compared to the ligament size; —, $29\,\mathrm{m\,s^{-1}}$; – – –, $38\,\mathrm{m\,s^{-1}}$; · · ·, $50\,\mathrm{m\,s^{-1}}$.

The droplet diameters d are more broadly distributed and present a skewed distribution. When the sizes are rescaled by d_0, which depends on u_2 as explained above, their distribution $p_B(d/d_0)$ keeps roughly the same shape for various air flows (figure 16*b*). The average droplet size resulting from the breakup of a ligament is $d \simeq 0.4 d_0$.

3.6. *In the spray*

The breakup process described above is often referred to as 'primary breakup'. If drops produced by this process are big enough (precisely, if the Weber number constructed with their size and the relative velocity they have with the air stream is larger than about 10 (Hanson *et al.* 1963), they may break again, in a 'secondary atomization' process. That second stage is virtually absent in the present case. The reason for this lies in the axisymmetric configuration of the air jet, which expands and therefore slows down for downstream distances larger that about 4–5 air gap thicknesses e (the length of the air jet potential core). The velocity contrast between the gas and the primary droplets thus shrinks rapidly and the distribution of droplet sizes issuing from the ligament breakup is essentially frozen (Marmottant 2001). The global size distribution function $p(d)$ in the spray is thus a mixture of the contributions coming from different ligaments, each characterized by their own frozen size distribution $p_L(d/d_0)$.

The window for measuring the global size distribution function $p(d)$ in the spray was chosen downstream of the ligament breakup region, far enough first to let the biggest droplets relax towards a spherical shape, and second to let the spray dilute in the air stream, therefore maximizing the efficiency of our droplet detection procedure (figure 17).

The procedure is described in Appendix A. We use a large-aperture small depth of field (of the order of 1 mm) lens and an image analysis algorithm which detects in-focus and isolated droplets only. Their size is computed from their projected area on the images, provided their projected shape is close enough to a disk. Statistics typically involved 2000 uncorrelated images of the spray, representing a set of 10^4 different droplets for each case.

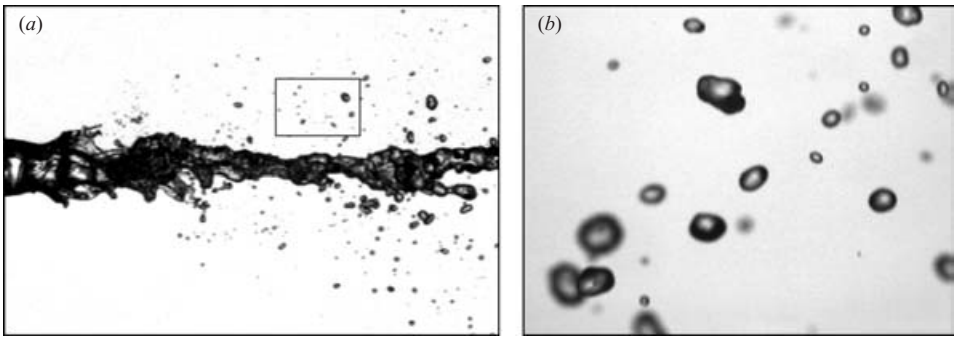

FIGURE 17. (*a*) Images in the spray after ligament breakup, (*b*) sample of the images used to detect droplets.

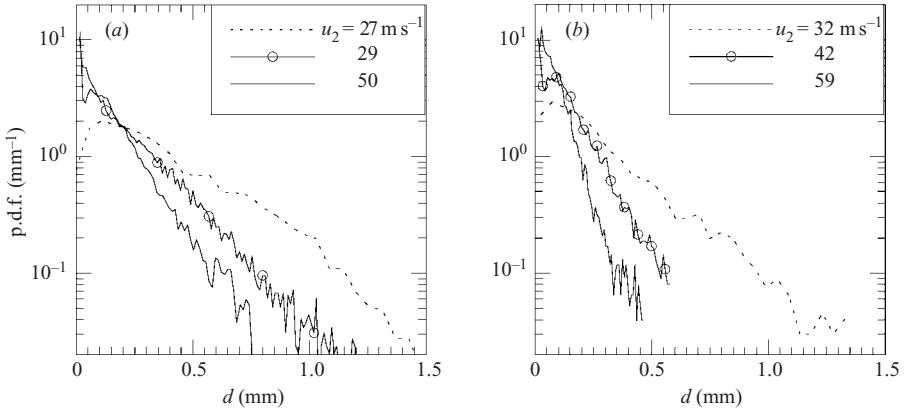

FIGURE 18. Droplet size distributions in the spray: (*a*) water (*b*) glycerol solution.

The droplet size distribution $p(d)$ (figure 18) displays an exponential fall-off at large diameters solely parameterized by the average ligament size $\langle d_0 \rangle$:

$$p(d) \sim \exp(-nd/\langle d_0 \rangle), \tag{3.3}$$

the parameter $n \approx 3.5$ being slowly increasing with the air velocity. The mean droplet size in the spray, $d_{10} = \int \mathrm{d}p(d)\,\mathrm{d}d$, decreases like u_2^{-1} (figure 19*a*), like $\lambda_\perp$ and $\langle d_0 \rangle$. For water, the proportionality relation is $d_{10} \simeq 0.10\lambda_\perp$, for ethanol $d_{10} \simeq 0.08\lambda_\perp$. These values are consistent with observations at the scale of each ligament, which concluded in a mean droplet size of $0.4d_0$ after a ligament breakup, together with an average ligament size of $\langle d_0 \rangle \simeq 0.23\lambda_\perp$.

The use of a viscous glycerol solution instead of pure water changes both the ligament aspect ratio at breakup (see e.g. figure 34*b*), the droplet size and its dependence on the air velocity (figure 18*b*). Ligaments are more elongated, thinner in diameter and break into smaller droplets. This difference relative to the pure water case amplifies with increasing air velocity (figure 19*b*).

4. Analysis

The experimental findings of the previous section suggest that a succession of instabilities is responsible for the transformation of the liquid from a round jet to a set of dispersed droplets. We examine now the underlying physical mechanisms.

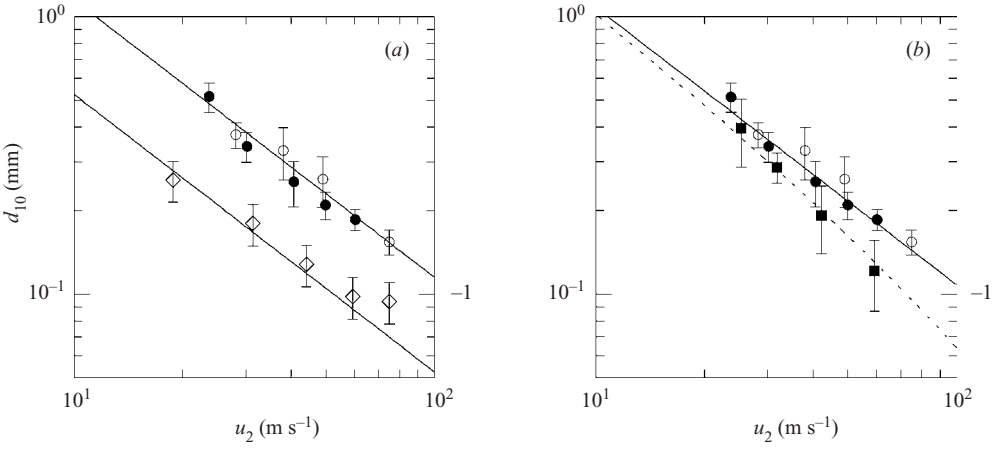

FIGURE 19. Mean diameter in the spray; (*a*) water, ●, $u_1 = 0.45\,\mathrm{m\,s^{-1}}$; ○, $u_1 = 0.94\,\mathrm{m\,s^{-1}}$; and ethanol, ◇, $u_1 = 0.5\,\mathrm{m\,s^{-1}}$. (*b*) water, and glycerol solution, ■, $u_1 = 0.35\,\mathrm{m\,s^{-1}}$.

4.1. *Shear instability*

Two initially parallel streams having different velocities are naturally unstable: this is the Kelvin–Helmholtz paradigm. The mode selection of the instability involves detailed properties of the separation interface between the streams, such as its surface tension or its thickness if the crossover between the fast and slow stream is not made abruptly. Both of these ingredients exist and we give below a discussion of the relevant limit in the present case.

4.1.1. *Thin vorticity layer: the Kelvin–Helmholtz limit*

Consider a velocity discontinuity, thus presenting a vanishingly small vorticity thickness ($\delta \to 0$), separating two potential flows with constant velocity. The dispersion relation of two-dimensional small-amplitude waves $\xi = |\xi| \exp(\mathrm{i}kx - \mathrm{i}\omega t)$ is

$$\omega = k\frac{\rho_1 u_1 + \rho_2 u_2}{\rho_1 + \rho_2} \pm \mathrm{i}\frac{k}{\rho_1 + \rho_2}\sqrt{\rho_1\rho_2(u_2 - u_1)^2 - (\rho_1 + \rho_2)\sigma k}, \tag{4.1}$$

in the absence of gravity (Chandrasekhar 1961). Assuming a spatially uniform perturbation ($\mathrm{Im}(k) = 0$), the temporal growth rate $\omega_i = \mathrm{Im}(\omega)$, is proportional to k for small wavenumbers and surface tension is stabilizing at large k, i.e. for

$$k > k_c = \frac{\rho_1\rho_2}{\rho_1 + \rho_2}\frac{(u_2 - u_1)^2}{\sigma}.$$

For a liquid–gas interface ($\rho_1 \gg \rho_2$), with a large velocity difference ($u_2 \gg u_1$), the most amplified mode and group velocity are

$$k_m = \frac{2}{3}\frac{\rho_2 u_2^2}{\sigma}, \qquad \frac{\partial\omega}{\partial k} = u_1 + \frac{\rho_2}{\rho_1}u_2. \tag{4.2}$$

The above result is, however, of little practical interest in a large variety of situations.

4.1.2. *Non-zero vorticity layer: the Rayleigh limit*

A way to produce a shear between two parallel streams is to accelerate them in distinct channels separated by a rigid boundary. The method implies the formation of boundary layers at the wall of the conveying channels resulting in thickened

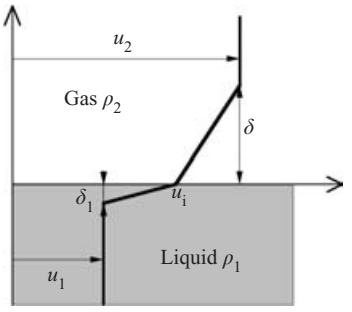

FIGURE 20. Linear velocity profile used in the instability analysis.

velocity profiles at their merging location. Additional lengthscales to the one formed by the ratio of surface tension to inertia $\sigma/\rho_2 u_2^2$ appear in the problem, namely the boundary-layer thicknesses δ and δ_1 (figure 20). The impact of a finite-size vorticity thickness at the interface between two streams of equal densities was first analysed by Rayleigh (1880) showing that the selection of mode is actually realized by this thickness. Rayleigh showed also that the instability of inflectional velocity profiles has not, by contrast with the boundary-layer type of profile, a viscous origin, and the way in which viscosity weakens the growth rate at very low Reynolds number was quantified later (see e.g. Betchov & Szewczyk 1963).

One of the subtleties of the present problem is that it incorporates two phases, with (very) different densities and viscosities and thus, *a priori*, different vorticity thicknesses. However, only one is important in the present limit of a fast gas phase contacting a nearly quiescent liquid through a thick layer δ.

A very short time after the streams have merged, the overall velocity profile can be sketched as in figure 20. The continuity of viscous stress τ across the interface is written as

$$\tau = \eta_2 \frac{u_2 - u_i}{\delta} = \eta_1 \frac{u_i - u_1}{\delta_1}, \tag{4.3}$$

with η_1 and η_2 the viscosities of each phase and u_i the velocity at the interface. In this parallel stream approximation, the liquid layer can only grow by viscous diffusion so that $\delta_1 \sim \sqrt{\nu_1 t}$.

Since $u_2 \gg u_1$, we have $\eta_2(u_2 - u_i)/\delta \approx \eta_2 u_2/\delta$ and $u_i - u_1 = (\eta_2 u_2/\eta_1\delta)\sqrt{\nu_1 t}$. The Reynolds number based on the gas shear-layer thickness $Re_\delta = u_2\delta/\nu_2$ is of the order of 500 in the present experiment, much larger that the value below which the damping role of viscosity starts to be effective which is about 100 (Betchov & Szewczyk 1963; Villermaux 1998*b*). It takes some time, however, for the liquid shear layer to reach this condition. With $Re_1 = (u_i - u_1)\delta_1/\nu_1 = Re_\delta(\eta_2/\eta_1)(\nu_2 t/\delta)$, this time, for a water–air system and with $Re_\delta = u_2\delta/\nu_2 = 500$ is approximately

$$\frac{\nu_2 t}{\delta^2} = 10. \tag{4.4}$$

As will be show below, the growth rate of the overall inflectional profile, neglecting completely the contribution of the liquid layer (i.e. setting $\delta_1 = 0$), is $\rho_2 u_2/\rho_1\delta$ so that the instability based on the gas profile solely has, by the time the above condition is reached, developed by $10 \times (\delta^2/\nu_2)(\rho_2 u_2/\rho_1\delta) = 5$ turnover times. This is, by far, enough to study a generic profile such as that of figure 20 with $\delta_1 = 0$. This broken line profile is a caricature of the actual continuous velocity profile known, in one-phase flows, to capture all the physics (wavenumber cut-off, growth rate) of the

instability (Huerre & Rossi 1998). This type of profile has an analytic dispersion relation which is conveniently manipulated. Using dimensionless variables $\kappa = k\delta$ and $\Omega = \omega\delta/(u_2 - u_1)$, the dispersion relation is (Villermaux 1993, 1998*a*; Raynal *et al.* 1997)

$$\mathrm{e}^{-2\kappa} = \left[1 - 2\left(\Omega + \kappa\frac{u_2/u_1}{u_2/u_1 - 1}\right)\right] \times \frac{1 + \left(\dfrac{\rho_1}{\rho_2} + 1\right)\left(\Omega + \dfrac{\kappa}{u_2/u_1 - 1}\right) - \dfrac{\kappa^3}{We}\left(\Omega + \dfrac{\kappa}{u_2/u_1 - 1}\right)^{-1}}{1 + \left(\dfrac{\rho_1}{\rho_2} - 1\right)\left(\Omega + \dfrac{\kappa}{u_2/u_1 - 1}\right) - \dfrac{\kappa^3}{We}\left(\Omega + \dfrac{\kappa}{u_2/u_1 - 1}\right)^{-1}}, \quad (4.5)$$

where $We = \rho_2(u_2 - u_1)^2\delta/\sigma$ is the Weber number based on the gas shear-layer thickness δ.

4.1.3. *Thick vorticity layer*

The vanishingly small vorticity-layer limit has been studied in § 4.1.1. Conversely, in the large Weber number *We* limit, corresponding for instance to a thick vorticity layer, factors containing $1/We$ are negligible and the stability properties of the layer are then described by the dispersion equation studied by Villermaux (1993, 1998*a*) as a direct extension of the Rayleigh approach, incorporating density differences

$$\mathrm{e}^{-2\kappa} = [1 - (2\Omega^* + \kappa)]\frac{1 + \frac{1}{2}(\rho_1/\rho_2 + 1)(2\Omega^* - \kappa)}{1 + \frac{1}{2}(\rho_1/\rho_2 - 1)(2\Omega^* - \kappa)}, \quad (4.6)$$

with $\Omega^* = \Omega - 2\kappa(u_2 + u_1)/(u_2 - u_1)$ in the reference frame moving at the average velocity $(u_1 + u_2)/2$. Setting $\omega = \omega_r + \mathrm{i}\omega_i$, the temporal stability analysis of 4.6 displays a growth rate $\omega_i(k)$ tangent to the velocity discontinuity dependence at small k (i.e. $\omega_i(k) \sim k(\rho_2/\rho_1)^{1/2}(u_2 - u_1)$, see (4.1)) and an overall bell-shape with a cut-off at $k_c = 2(\rho_2/\rho_1)^{1/2}/\delta$.

The most amplified wavenumber and associated growth rate are (for $u_2 \gg u_1$)

$$k_m \simeq 1.5\left(\frac{\rho_2}{\rho_1}\right)^{1/2}\frac{1}{\delta}, \qquad \omega_i(k_m) \simeq \frac{\rho_2}{\rho_1}\frac{u_2}{\delta}. \quad (4.7)$$

The group velocity at k_m is very well represented by a convection velocity u_c estimated from stress continuity at the interface (Bernal & Roshko 1986; Dimotakis 1986)

$$\left(\frac{\partial\omega}{\partial k}\right)_{k_m} \simeq u_c = \frac{\sqrt{\rho_1}\,u_1 + \sqrt{\rho_2}\,u_2}{\sqrt{\rho_1} + \sqrt{\rho_2}}, \quad (4.8)$$

within 10% accuracy in the air/water case with $\rho_2/\rho_1 = 1.2/1000$.

The wavelength λ is prescribed by the vorticity thickness and density ratio $\delta(\rho_1/\rho_2)^{1/2}$, the passage frequency of the birthing surface undulations is given by $f \sim u_c/\delta$ with a temporal growth rate $\omega_i(k_m) \sim u_2/\delta(\rho_2/\rho_1)$.

The transposition of the above results to a spatial growth, as is the case in this convected flow, setting ω real and $k = k_r + \mathrm{i}k_i$, owing to the Gaster (1962) transformation $k_i = \omega_i/u_c$, provided $\omega_i(k_m)/f \ll 1$ in the temporal analysis.

We have

$$\omega_i(k_m)/f = \frac{2\pi}{1.5}\left(\frac{\rho_2}{\rho_1}\right)^{1/2}\frac{M^{1/2}}{M^{1/2} + 1},$$

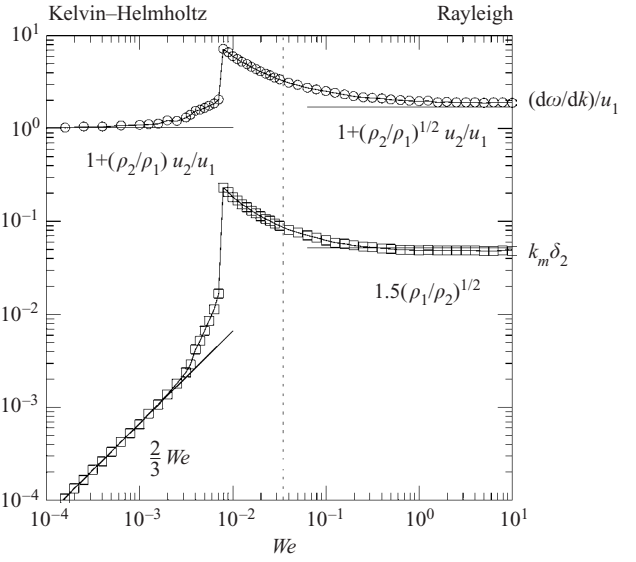

FIGURE 21. Transition from a thin shear layer and a large layer as a function of the Weber number at $u_2/u_1 = 20$; ○, group velocity; □, most unstable wavenumber; - - -, $We = (\rho_2/\rho_1)^{1/2}$.

with $M = \rho_2 u_2^2/\rho_1 u_1^2$ the momentum ratio between the streams. Since $\rho_2 \ll \rho_1$, and $M > 1$ in the present experiments, $\omega_i(k_m)/f \ll 1$ is never larger than about 0.14, thus fulfilling the Gaster requirement.

4.1.4. *Transition between the two limiting cases*

The numerical solution of the complete dispersion equation, (4.5), shows, as expected, a transition from the thin vorticity layer ($We \ll 1$) to the thick vorticity layer ($We \gg 1$). The selected wavenumber is indeed $k_m = 2\rho_2 u_2^2/3\sigma$ for small We, and tends to $k_m = 1.5(\rho_1/\rho_2)^{1/2}/\delta$ at large We. The group velocity $\partial\omega/\partial k$ jumps from nearly u_1 to u_c when the Weber number increases, after a discontinuous transition (see figure 21).

That transition occurs for

$$We \sim \left(\frac{\rho_2}{\rho_1}\right)^{1/2}. \tag{4.9}$$

Even in the presence of surface tension, the shear does not affect the layer for wavelengths shorter that $\delta(\rho_1/\rho_2)^{1/2}$. The Rayleigh mode selection thus overcomes the pure Kelvin–Helmholtz one as long as $\sigma/\rho_2 u_2^2 < \delta(\rho_1/\rho_2)^{1/2}$, hence providing condition, (4.9) above (Villermaux 1998*a*).

Note, finally, that this shear instability overcomes the capillary instability of the jet itself as soon as its growth rate $u_2/\delta \times \rho_2/\rho_1$ is larger than the capillary growth rate $(\sigma/\rho_1 D_1^3)^{1/2}$, that is when $We_\delta \gg \rho_1/\rho_2 \times (\delta/D_1)^3$, a condition always fulfilled in these experiments.

4.1.5. *Comparison with experiments*

In the experiments described in § 3, $We(\rho_1/\rho_2)^{1/2}$ was always larger than 50 so that the large-vorticity-layer description holds. The ratio of the selected wavelength λ to δ is indeed observed to be constant (see figure 5*a*).

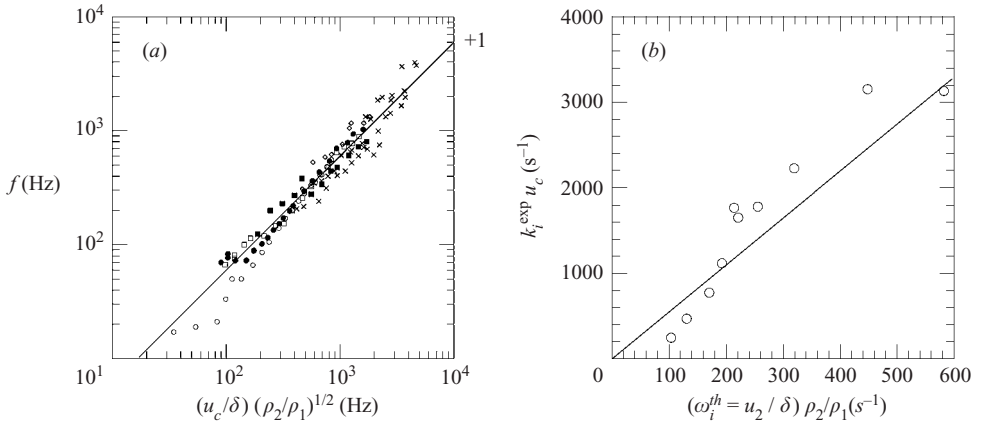

FIGURE 22. (*a*) Measured frequency as a function of the predicted dependency in the parameters of the flow; ○, $u_1 = 0.20\,\mathrm{m\,s^{-1}}$; ●, $0.32\,\mathrm{m\,s^{-1}}$; □, $0.45\,\mathrm{m\,s^{-1}}$; ■, $0.80\,\mathrm{m\,s^{-1}}$; ◇, $1.69\,\mathrm{m\,s^{-1}}$; ×, results of Eroglu & Chigier (1991). (*b*) Estimation of the temporal growth rate, according to the Gaster transformation of the spatial growth rate, as a function of the theoretical prediction ω_i^{th}. Lines show linear fits.

The small effect of the liquid velocity on this ratio is a convergence effect due to gravity which enlarges the gas boundary-layer thickness at small liquid velocities because the liquid surface is not parallel to the gas jet in that case. This, in turn, increases the selected wavelength slightly.

The passage frequency f is well accounted for by a proportionality to u_c/δ as the good collapse obtained on figure 22*a* suggests. Also shown in this figure are the frequency measurements of Eroglu & Chigier (1991). Those were made on a similar coflowing set-up, with a convergent air channel. The liquid jet diameter was $D_1 = 0.971\,\mathrm{mm}$, and the annulus gap of $h = 4.55\,\mathrm{mm}$ at the exit. Assuming a boundary-layer development in the gas stream similar to our case (equation (2.2)), their results nicely fit ours, and extend them to higher frequencies. The frequency f is proportional to the gas velocity raised at the power 3/2, this exponent being decomposed in 1 for the dependence of u_c on u_2 at high gas velocity plus 1/2 for the dependence of the shear-layer thickness δ on u_2 (see equation (2.2)).

Using a planar air/water shear layer, Raynal *et al.* (1997) recovered these trends. These authors were also able to measure the convection velocity u_c which showed a good agreement with equation (4.8).

The spatial growth of the undulations is initially exponential, $\sigma_{\mathrm{rms}} \sim \exp(k_i x)$. The temporal growth rate, estimated by the Gaster relation $\omega_i(k_m) = k_i u_c$ is proportional to the predicted growth rate $\omega_i(k_m) \simeq u_2/\delta \times \rho_2/\rho_1$ (figure 22*b*).

The predictions of the stability analysis are consistent with the observed dependencies on velocities and boundary-layer thickness; however, the prefactors are not, as can be seen on table 2. The difference is attributed to the way the velocity profile has been caricatured. The vorticity is not constant in the experimental boundary layer, contrary to the linear profile used in the stability analysis. The effective linear boundary-layer thickness to use in a prediction that matches experimental results is 4 to 6 times larger. This is consistent with the fact that experimental profiles are smoother than a broken line profile. A stability analysis with a constant vorticity on width δ thus gives a higher bound for the quantities shown on table 2.

		Experiments (E)	Stability analysis (S)	Ratio (S)/(E)
Wavelength	$\lambda/\left(\delta\left(\frac{\rho_1}{\rho_2}\right)^{1/2}\right)$	1.0–1.4	4.2	4–3
Frequency	$1/f\left(\frac{\delta}{u_c}\left(\frac{\rho_1}{\rho_2}\right)^{1/2}\right)$	1.4	4.2	3
Growth rate	$1/\omega_i(k_m)\left(\frac{\delta}{u_2}\frac{\rho_1}{\rho_2}\right)$	0.17	1	6

TABLE 2. Comparison with the the linear stability analysis with a linear velocity profile of thickness δ.

4.2. *Transverse destabilization*

Several mechanisms have been proposed in related contexts to account for the formation of corrugations, ligaments and then droplets at the surface of liquid jets with and without coflow.

The azimuthal secondary instability of the primary wave crests differs from the primary destabilization in two ways. First, the azimuthal wavelength $\lambda_\perp$ depends on surface tension when the distance between the primary crests λ does not and secondly, $\lambda_\perp$ is proportional to u_2^{-1} and not to $\delta \propto u_2^{-1/2}$. A spanwise destabilization of the mixing layer is therefore unlikely, because it would produce transverse wavelengths proportional to the primary ones (see e.g. Bernal & Roshko 1986).

For a laminar jet issuing in a still atmosphere with a relative velocity Δu, Wu, Ruff & Faeth (1991) proposed that the boundary layer formed in the liquid with a depth $\delta_1 \sim \sqrt{\nu_1 t}$, and as it destabilizes and is torn-off from the liquid bulk, forms ligaments and droplets. Assuming that it detaches at a distance of order of the diameter of the injector, these authors infer that the ligament and drop size is $D_1 Re_1^{-1/2}$. This size does not depend on liquid surface tension and varies proportionally to $\Delta u^{-1/2}$. This provides satisfactory scaling relations for liquid density and viscosity, but not velocity since their measurements rather show a variation of the droplet sizes like $\Delta u^{-0.77}$.

By analogy with drop breakup in an airstream, we can imagine that the balance between aerodynamic pressure $\rho_2 u_2^2$ and capillary pressure σ/d sets a size for the fragments peeled-off from the liquid $d \sim \sigma/(\rho_2 u_2^2)$ corresponding to a constant Weber number constructed on d (Lasheras & Hopfinger 2000). Surface tension then plays a role, although the detailed mechanism of breakup is not explicit. The dependence on the relative velocity is very strong in that scenario, i.e. Δu^{-2}.

The crest shapes become singular as the primary waves grow in amplitude, marking the birth of a liquid sheet, bounded by a rim. The capillary instability of the rim has been proposed as a possible mechanism for the origin of the transverse modulations (Villermaux 1998*a*). However, experiments show that this modulation occurs very early, nearly concomitantly with the formation of the primary undulations, before a sheet has developed significantly. Moreover, the capillary time constructed on λ, or even a fraction of λ, is always larger than the primary instability turnover time.

Studying flapping liquid sheets, Villermaux & Clanet (2002) have proposed that the unsteady motions at the sheet rim confer transient accelerations to the liquid which trigger a Rayleigh–Taylor type of instability, producing indentations of the rim,

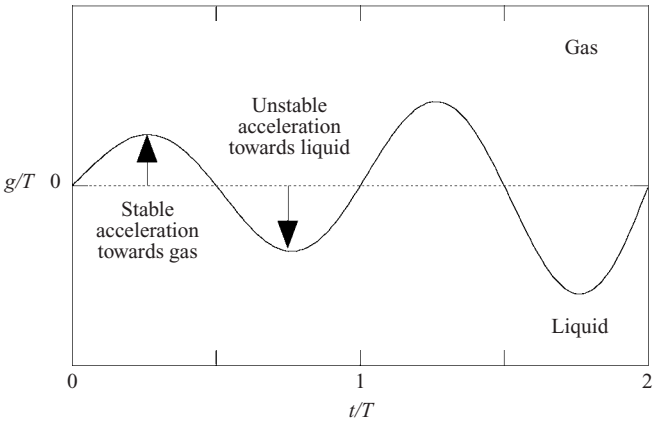

FIGURE 23. Surface acceleration.

ligaments, and then drops. Their scenario fits well with the measurements involving different liquid surface tensions and ambient gas densities.

We suggest in the following that the accelerations that the liquid interface suffers perpendicular to itself at the passage of the travelling primary undulations become rapidly large enough to produce a secondary instability.

4.2.1. *Surface acceleration*

According to the analysis of § 4.1.3, the surface undulations coming from the primary shear instability propagate with a group velocity $u_c \approx u_1 + u_2(\rho_2/\rho_1)^{1/2}$ (since $\rho_2/\rho_1 \ll 1$) in the laboratory frame, a velocity which is larger than the liquid bulk velocity u_1. The discussion of § 4.1.2 also suggests that the interfacial velocity u_i is not appreciably different from u_1 after one instability turnover time. We therefore neglect the friction acceleration of the surface, and set $u_i \approx u_1$.

The undulations of wavelength λ, moving at a velocity $u_c - u_1$ have a pulsation

$$\omega_L = \omega - ku_1 = 2\pi\frac{u_c - u_1}{\lambda} \approx 2\pi\sqrt{\frac{\rho_2}{\rho_1}}\frac{u_2}{\lambda}, \tag{4.10}$$

in the frame of the liquid, the 'Doppler shift' $-ku_1$ being non-negligible at small gas velocity only. We used (4.8) to express the group velocity.

The shear perturbation amplitude is initially growing with a growth rate ω_i ($\approx 2/3\,\omega_L$) and saturates at an amplitude a (see figure 6*b*). Then transverse digitations start to grow. The interface of elevation $\xi = -a\sin(\omega_L t)$, is then subjected to a perpendicular acceleration

$$g = \frac{\mathrm{d}^2\xi}{\mathrm{d}t^2} = a\,\omega_L^2\sin(\omega_L t). \tag{4.11}$$

This acceleration is quite large in practice, with $u_1 = 1\,\mathrm{m\,s^{-1}}$ and $u_2 = 20\,\mathrm{m\,s^{-1}}$ the wave frequency is 200 Hz in the laboratory frame and 100 Hz in the liquid frame. For a typical wave amplitude of $a = 1$ mm, the acceleration of the surface is $g = 400\,\mathrm{m\,s^{-2}}$, much larger than the acceleration due to gravity.

4.2.2. *Rayleigh–Taylor instability*

The acceleration of the interface is oscillatory, alternatively aimed in the direction of the gas and of the liquid (figure 23). When the acceleration is oriented towards

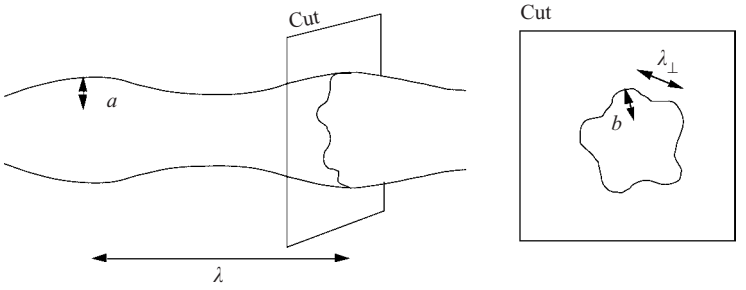

FIGURE 24. Development of the transverse instability.

the heavier phase, it is unstable in the sense of Rayleigh–Taylor (Rayleigh 1883; Lewis 1950; Taylor 1950). Since elevation and acceleration are in phase opposition (equation (4.11)), this situation occurs when the wave elevation is around its maximum above the liquid. An azimuthal perturbation, transverse to the primary crests $b = b_0 \exp(im\phi)$ (figure 24) can thus be amplified.

For a plane surface submitted to a constant acceleration level g, the Rayleigh–Taylor instability as a temporal growth rate and a maximum amplified wavelength is given by

$$\omega_{i\,RT} = \left(\frac{2}{3\sqrt{3}}\right)^{1/2} \left(\frac{\rho_1 g^3}{\sigma}\right)^{1/4}, \tag{4.12}$$

$$\lambda_{RT} = 2\pi \left(\frac{3\sigma}{\rho_1 g}\right)^{1/2}, \tag{4.13}$$

when $\rho_1 \gg \rho_2$ (see e.g. Chandrasekhar 1961). These orders of magnitude are useful for the present experiment when the spacings of the azimuthal undulations are small in comparison to the jet perimeter. The acceleration varies in the unstable subset of one oscillating cycle, and the net growth of a perturbation can be estimated by

$$b_1 = b_0 \exp \int_0^{T_L/2} \omega_{i\,RT}(t)\,\mathrm{d}t, \tag{4.14}$$

where $T_L = 2\pi/\omega_L$. Liquid ligaments will develop if the amplification factor b_1/b_0 is large enough, that is if the duration and amplitude of the acceleration is large enough, in other words if

$$\int_0^{T_L/2} \omega_{i\,RT}(t)\,\mathrm{d}t \sim \frac{1}{\omega_L}\left(\frac{\rho_1 g_{\max}^3}{\sigma}\right)^{1/4} \sim \left(\left(\frac{a}{\lambda}\right)^3 We_\lambda\right)^{1/4}, \tag{4.15}$$

is larger than a critical value. $We_\lambda = \rho_2 u_2^2/(\sigma/\lambda)$ stands for the Weber number constructed on λ. This threshold is determined experimentally by the simultaneous observation of the amplitude and wavelength of the primary undulations at the critical conditions when ligaments appear (figure 25). The quantity $a/\lambda \times We_\lambda^{1/3}$ increases with air velocity and ligaments begin to form when the air velocity exceeds about $21\,\mathrm{m\,s^{-1}}$, when $a/\lambda \times We_\lambda^{1/3}$ is larger than about $\beta = 0.5$. The critical amplitude is thus

$$\frac{a_c}{\lambda} = \beta We_\lambda^{-1/3}. \tag{4.16}$$

Another possible derivation of the above critical condition consists in assuming that the azimuthal instability will develop with a substantial net growth when the inverse

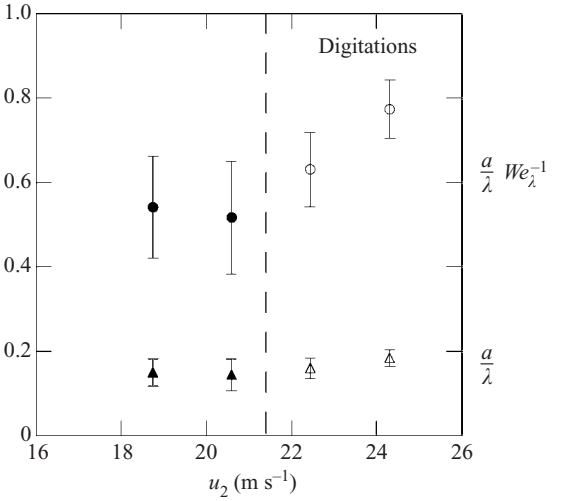

FIGURE 25. ▲, measured maximum amplitude of longitudinal waves on the jet; ●, expected amplification of the Rayleigh–Taylor instability (at the power four), based on measured quantities (see equation (4.15)). Solid symbols, no digitations grow; open, digitations, grow; $u_1 = 1\,\mathrm{m\,s^{-1}}$.

of the Rayleigh–Taylor growth rate based on the maximal acceleration level $a(u_2/\lambda)^2$ is of the order of the transit time λ/u_c of the wave responsible for the acceleration of the interface.

At this amplitude, the maximum acceleration of the interface is $g_{\max} = a_c\omega_L^2$, and according to (4.13) the selected wavelength is of the order

$$\lambda_\perp = 2\pi\left(\frac{3\sigma}{\rho_1 g_{\max}}\right)^{1/2} = \lambda\, We_\lambda^{-1/3}\left(\frac{3}{\beta}\right)^{1/2}. \tag{4.17}$$

Expressed as a function of the vorticity thickness δ (using the experimental value for the wavelength $\lambda \simeq 1.2(\rho_1/\rho_2)^{1/2}\delta$, and the threshold parameter $\beta = 0.5$), the ligament spacing is expected to scale as

$$\lambda_\perp \simeq 2.8\,\delta\, We_\delta^{-1/3}\left(\frac{\rho_2}{\rho_1}\right)^{-1/3}. \tag{4.18}$$

Figure 26 shows that the experimental data collapse reasonably well on this prediction, in trend and in absolute value. Particularly, the effect of surface tension is well accounted for. According to (4.18), the spacing is independent of liquid viscosity, as is indeed observed. At low Weber numbers, the measured wavelengths do not match the prediction, because the assumption of plane interface does not hold when the transverse wavelength is not small compared to the jet perimeter (see figure 9). For smaller wavelengths, the plane interface hypothesis holds.

In the present particular geometry where the gas stream is an annular jet of initial width e, the shear instability will develop with the expected features up to the amplitude given in (4.16) provided the primary wavelength λ is smaller than the downstream distance above which the gas stream decreases, that is, the gas potential core length. It is about 5 or 6 times h long. With $\lambda \sim 30\,\delta \sim 170\,h\,Re^{-1/2}$, this condition yields a critical air velocity of $20\,\mathrm{m\,s^{-1}}$ (see figure 25).

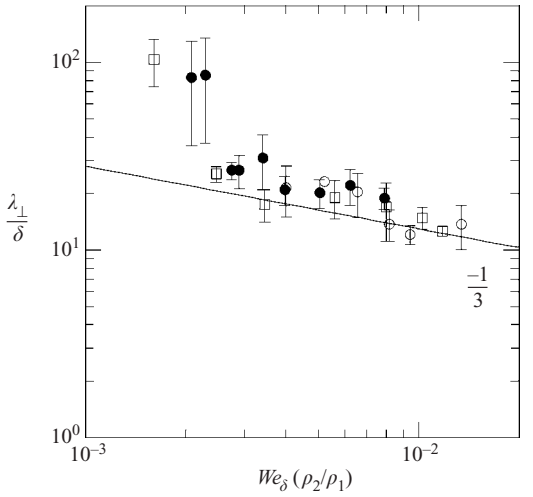

FIGURE 26. Transverse ligament size for three different liquids; ●, water; ○, ethanol; □, glycerol solution. —, prediction of equation (4.18).

4.3. *Acceleration of the crests*

The discussion above is confined to small interface corrugation amplitudes since it is a combination of results from linear stability analyses. This is an admissible restriction as long as the discussion aims at predicting lengths and timescales. However, once the amplitudes become appreciable, when the ligaments start to be accelerated in the fast gaseous stream, the dynamics, although it still relies on a balance of aerodynamic and capillary forces, has to be reformulated.

In a first phase, the crests of the liquid undulations are accelerated with respect to the liquid bulk as a whole, without much deformation. If v_x denotes the crest velocity in the streamwise direction, a force balance on the crest is written as

$$\rho_1 v_0 \frac{\mathrm{d}v_x}{\mathrm{d}t} = \tfrac{1}{2}\rho_2 u_2^2 C_D S - \sigma P, \tag{4.19}$$

where S is the surface of the crest facing the air flow and P the perimeter connecting the crest to the bulk of the liquid. The drag coefficient C_D does not depend much on u_2 at high Reynolds number (Schlichting 1987) which, estimated at the scale $\lambda_\perp$, is of order 8000.

The longitudinal and transverse dimensions of a corrugation are of the order of $\lambda_\perp$ and height above the bulk $a_c \sim \lambda_\perp$ at onset so that its volume scales as $v_0 \sim \lambda_\perp^3$, its surface as $S \sim \lambda_\perp^2$ and perimeter as $P \sim \lambda_\perp$. Given these estimates, the ratio of aerodynamic forces to capillary forces in equation (4.19) is of order $We_{\lambda_\perp}$, whose value is typically larger than 50. Capillarity is thus negliglible and the crest acceleration is given by

$$\frac{\mathrm{d}v_x}{\mathrm{d}t} \sim \frac{\rho_2 {u_2}^2}{\rho_1 \lambda_\perp}. \tag{4.20}$$

To this temporal acceleration corresponds a spatial acceleration $\mathrm{d}v_x/\mathrm{d}t = v_x(\mathrm{d}v_x/\mathrm{d}x)$. Initially $v_x = u_1$, and then $\mathrm{d}v_x/\mathrm{d}x = \mathrm{d}v_x/\mathrm{d}t/u_1$. Since $\lambda_\perp \sim u_2^{-1}$, the spatial increase of the velocity $\mathrm{d}v_x/\mathrm{d}x$ thus scales as ${u_2}^3/u_1$, as expected from figure 11(*b*).

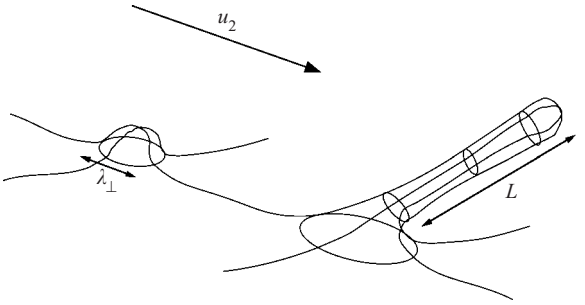

FIGURE 27. Sketch of a transverse modulation acceleration and ligament elongation.

4.4. *Ligament dynamics*

The subsequent evolution of the interface corrugations obeys the very same dynamics. The air drag pulls a crest from the liquid bulk, by amplifying its length and preserving its azimuthal symmetry, therefore forming a ligament of increasing length L (figure 27). If the characteristic elongation time $t_L = (\mathrm{d}\ln L/\mathrm{d}t)^{-1}$ is small compared to the emptying time of the ligament, given by the capillary time based on its initial size $\lambda_\perp$, i.e. $t_\sigma = (\rho_1\lambda_\perp^3/\sigma)^{1/2}$, the ligament stretches in the air stream at constant volume (Marmottant & Villermaux 2004). We have called this volume $v_0 = \pi d_0^3/6$, with $\langle d_0\rangle \simeq 0.23\lambda_\perp$.

The axial momentum of a volume in uniform extension is $p = \rho_1 v_0(\mathrm{d}L/\mathrm{d}t)/2$ and the balance of the forces acting on a ligament is

$$\tfrac{1}{2}\rho_1 v_0 \frac{\mathrm{d}^2 L}{\mathrm{d}t^2} = \tfrac{1}{2}\rho_2 u_2^2 C_D S - \sigma P, \tag{4.21}$$

with $S \simeq \pi d_0^2/4$ and $P \simeq \pi d_0$ the initial area and perimeter of the ligament cross-section, respectively.

The ratio of aerodynamic forces to capillary forces given by $We_{d_0}C_D/8$ is, again, large, since We_{d_0} is always larger than 15, and C_D of order unity (remember that the drag acts essentially at the tip of the ligament (Schlichting 1987). Capillarity is thus neglected in equation (4.21) which reduces to $\mathrm{d}^2L/\mathrm{d}t^2 = 3C_D(\rho_2 u_2^2/\rho_1 d_0)/2$. The ligament length follows a pure parabolic growth

$$\frac{L - L_0}{d_0} \simeq \frac{3C_D}{4}\left(\frac{t}{t_a}\right)^2, \tag{4.22}$$

with a characteristic time of acceleration

$$t_a = \frac{d_0}{u_2}\left(\frac{\rho_1}{\rho_2}\right)^{1/2}, \tag{4.23}$$

and $L_0 \simeq d_0$. Even though a more complete description, including the thinning of the ligament cross-section can be made, we see in figure 28 that the above trend is approximately followed, for different air velocities.

4.5. *Ligament breakup*

4.5.1. *Breakup length and diameter*

The ligaments detach from the liquid bulk by a pinching of their base. The time t_b it takes for the pinchoff to be completed is, as measured from time-resolved movies, close to the capillary time based on the ligament size d_0 (figure 29*a*), independent of

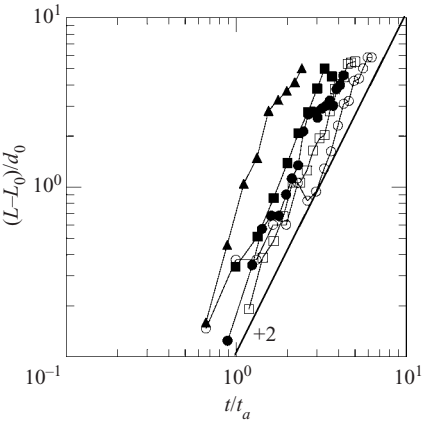

FIGURE 28. Length of ligaments as a function of the displacement time $t_a = d_0/u_2(\rho_1/\rho_2)^{1/2}$, ○, $u_2 = 25\,\mathrm{m\,s^{-1}}$; □, $29\,\mathrm{m\,s^{-1}}$; ●, $34\,\mathrm{m\,s^{-1}}$; ■, $40\,\mathrm{m\,s^{-1}}$; ▲, $50\,\mathrm{m\,s^{-1}}$.

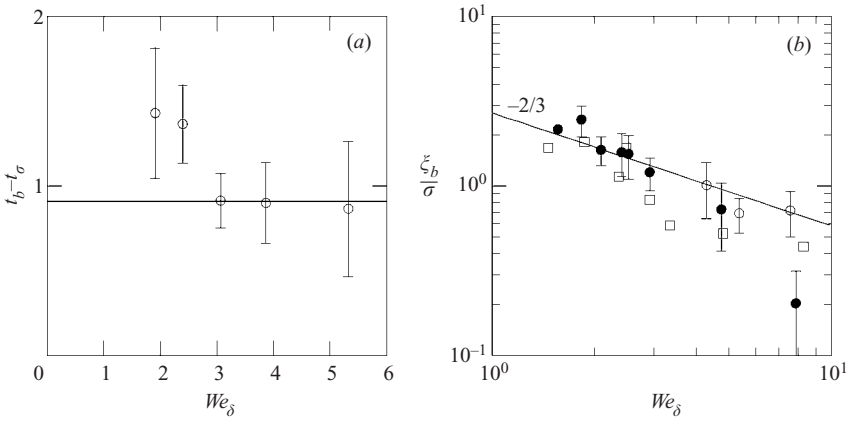

FIGURE 29. (*a*) Breakup time compared to the capillary time $t_\sigma = (\rho_1 {d_0}^3/\sigma)^{1/2}$. (*b*) Breakup diameter. ●, water; ○, ethanol; □, glycerol solution.

its rate of elongation

$$t_b \simeq t_\sigma = \left(\rho_1 d_0^3/\sigma\right)^{1/2}. \tag{4.24}$$

The reason of this distinct feature, also encountered in a different context (Marmottant & Villermaux 2004) is the existence at the ligament foot of a singular, unstreched region which behaves like a liquid bridge emptying on a capillary timescale.

The length L_b and thickness ξ_b at the breakup time are thus expected, from equations (4.22) to be

$$L_b/d_0 \sim (t_\sigma/t_a)^2 \sim We_{d_0}, \tag{4.25}$$

$$\xi_b/d_0 \sim (t_\sigma/t_a)^{-1} \sim We_{d_0}^{-1/2}, \tag{4.26}$$

with $We_{d_0} = \rho_2 u_2^2 d_0/\sigma$. The thickness ξ_b was inferred from the assumption of constant volume $v_0 = L\pi\xi^2/4 = \pi {d_0}^3/6$. Since d_0 is proportional to u_2^{-1} we have

$$L_b \sim {u_2}^0 = \text{const}, \tag{4.27}$$

$$\xi_b \sim u_2^{-3/2}. \tag{4.28}$$

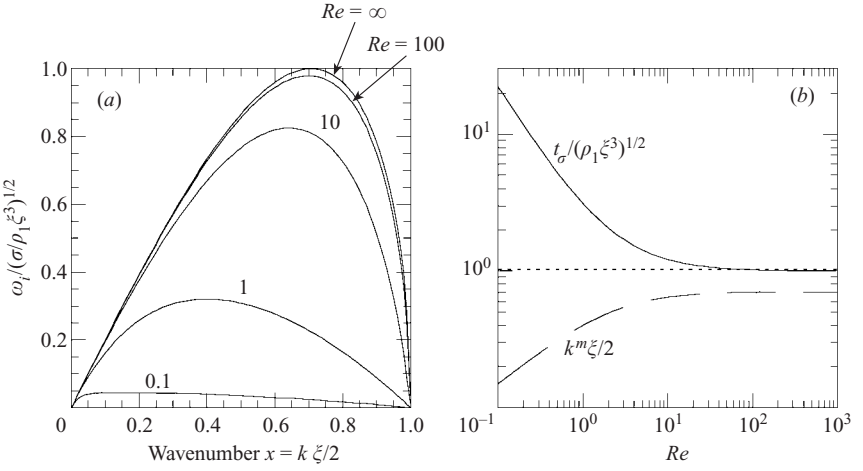

FIGURE 30. (*a*) Growth rate of the Plateau–Rayleigh instability as a function of Reynolds number. (*b*) – – –, wavenumber of maximum growth; —, capillary time to inviscid capillary time ($f(Re_\xi)$).

These two dependencies are seen on the figure 15 to fit all the more the experimental observations that the air velocity is high. Rewriting $d_0 \sim \lambda_\perp \sim \delta We_\delta^{-1/3}(\rho_1/\rho_2)^{1/3}$ in (4.26), we have

$$\xi_b \sim \delta\, We_\delta^{-2/3}\,(\rho_1/\rho_2)^{1/6}. \tag{4.29}$$

Figure 29(*b*) shows that equation (4.29) also accounts for surface tension effects. It is useful to note that a dependence such as $\xi_b \simeq 4\,\sigma/\rho_2 u_2{}^2$ corresponding to a constant Weber number based on ξ_b (i.e. $We_{\xi_b} \simeq 4$) would fit the experimental data equally well. This would correspond to an effective drag force proportional to $\rho_2 u_2^2 \xi_b^2$.

4.5.2. *Viscous slowing*

An increased liquid viscosity delays the pinching of the ligaments and their further breakup by slowing the capillary time. Ligaments thus break when they are more elongated, and therefore produce smaller droplets (see figure 19).

The capillary instability of an unstretched liquid cylinder is sensitive to viscosity in growth rate, and mode selection (see Chandrasekhar 1961; Eggers 1997). The growth rate ω_i in the range of unstable wavenumbers (whose limits are not affected by viscosity) is

$$\omega_i \simeq \sqrt{\frac{\sigma}{\rho_1\xi^3}}\left(\sqrt{4x^2(1-x^2)+\tfrac{9}{2}Re^{-2}x^4}-3\sqrt{2}Re^{-1}x^2\right), \tag{4.30}$$

where $x = k\xi/2$ is the wavenumber made dimensionless with the cylinder diameter ξ and $Re_\xi = \sqrt{\xi\sigma/2\rho_1\nu_1^2}$ a Reynolds number. The inverse of the maximal growth rate giving the effective breakup time is

$$t_\sigma = \frac{1}{\omega_i^m} = \sqrt{\frac{\rho_1\xi^3}{\sigma}}\,f(Re), \tag{4.31}$$

the function $f(Re_\xi)$, plotted in figure 30(*b*) being a decreasing function of Re, eventually approaching 1.

Experiments show that ligament diameters at breakup and mean droplet sizes (figures 19*b* and 29*b*) are somewhat smaller with a viscous glycerol solution than

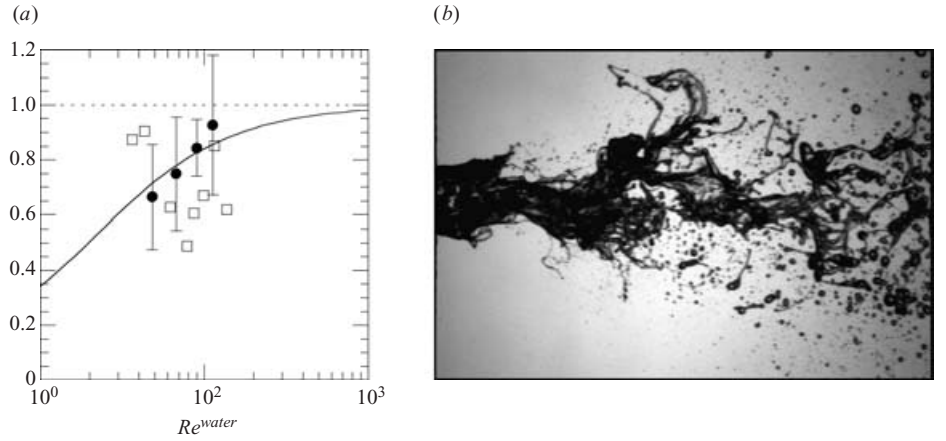

FIGURE 31. (*a*) □, $\xi_b^{gly}/\xi_b^{water}$, breakup diameters in the glycerol spray compared to the water spray, as a function of the Reynolds number based on the water diameters; ●, $d_{10}^{gly}/d_{10}^{water}$, mean droplet diameters in the glycerol spray compared to the water spray ; —, diameter ratio ξ^{gly}/ξ^{water} for which capillary growth are identical. (*b*) Image of the viscous jet showing long threads.

with pure water, the difference increasing with air speeds. This is consistent with the fact that, the ligament size being a decreasing function of air speed, the Reynolds number Re_ξ based on their size decreases, and therefore may reach values for which viscosity affects the breakup time through equation (4.31). For given conditions of air speed and liquid physical properties, ligaments break provided their capillary time is equal, that is, in particular, with a glycerol solution 12 times (kinematic viscosity) more viscous than pure water

$$t_\sigma\left(\xi_b^{gly}, 12\,\nu_1\right) = t_\sigma\left(\xi_b^{water}, \nu_1\right). \tag{4.32}$$

Ligament diameters ξ_b^{gly} realizing the above condition are of course smaller than those in pure water, as shown on figure 31(*a*). The mean droplet size in the spray follows a similar trend. This size is therefore not solely determined by the initial corrugation size $\lambda_\perp$ (or, equivalently, d_0), but also, through a weak correction, by the aspect ratio of the ligament at breakup.

5. Fragmentation

The broad size statistics is a fundamental characteristic of natural sprays formed in an uncontrolled way. Spume droplets, rain drops and fuel sprays all display a wide range of sizes, always with an exponential tail at large sizes. This may, at this stage, appear at odds with the fact that it is possible to identify typical lengthscales in the early stages of the interface destabilization process. The primary wavelength λ, the transverse width $\lambda_\perp$ of the digitations formed at the crest of the primary waves contain, in themselves, all the information on their formation process: their size is the typical size generated by the instability giving birth to them; but what is the typical droplet size in the spray on figures 17 and 18? The distribution is a continuous decreasing function of the size, and it is clear that the whole shape of the distribution has to be understood for itself.

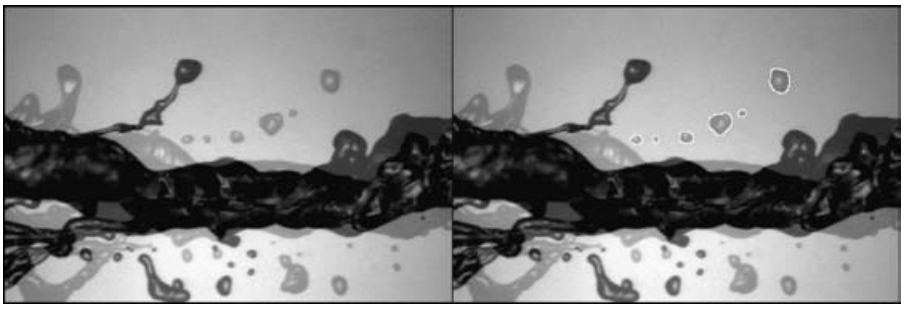

FIGURE 32. Double flash exposure of a ligament just before, and after breakup, and resulting droplets as captured by the detection algorithm.

5.1. *Droplet sizes from ligaments*

A key observation is that, although the ligaments detach from the liquid bulk with thickness ξ_b ($\propto u_2^{-3/2}$), they give rise to drops whose size is substantially larger, and scale as d_0 ($\propto u_2^{-1}$). In other words, no matter how thin a ligament is at breakup, it will form drops of the order of the size of the initial liquid surface corrugation which sets the ligament volume (see figure 16*b*).

As long as the ligament is attached to the liquid bulk and is stretched as described in § 4, the capillary instability of the ligament core is strongly damped. This is true for all modes whose instability rate is smaller than the stretching rate, as demonstrated by Frankel & Weihs (1985). However, as soon as the ligament has detached and is not (or much less) stretched, the capillary instability develops on a short timescale of the order, at most, of the capillary time based on the initial ligament size.

The reorganization of the liquid volume in the ligament while it stretches is a superposition of remnant motions from the liquid bulk, motions due to the transient growth and damping of capillary waves, motions induced by the deformation of the ligament owing to perturbations in the gas stream, etc... These are so complex that they are out of reach of a microscopic analysis. However, capillary forces are ultimately dominant and the liquid ligament fragments in several blobs.

We suggest that the blobs, just before breakup, interact, and that the interaction is of a *coalescence* or *aggregation* type. This view succeeds at predicting the overall drop size distribution in the spray. When two liquid blobs of slightly different sizes d_1 and d_2 are connected to each other, the smaller one (say d_1) aggregates the larger one owing to the Laplace pressures difference $\propto \sigma(1/d_1 - 1/d_2)$. The time it takes for the coalescence to be completed is of order $\sqrt{\rho d_1^3/\sigma}$ which is, also, the time it takes for the neck connecting the two blobs to destabilize and break. The resulting 'coalescence cascade' due to the confusion of these two timescales is nicely shown in Thoroddsen & Takehara (2000). For this reason, the blobs constitutive of the ligament tend, as they detach, to coalesce, thereby forming larger and larger blobs along the ligament. This is why the final drop size is larger than the thickness of the ligament ξ_b just after it has been released from the liquid bulk (figure 32).

Let $N(d, t)$ be the number of blobs constitutive of the ligament whose size is within d and $d + \mathrm{d}d$ at time t during the interaction period. The number of blobs of the same size an instant of time later $N(d, t + \Delta t)$ will result from the interaction of blobs of various sizes in the distribution $N(d, t)$. Provided the interaction is made at random, this evolution mechanism selects distributions $N(d, t)$ which are stable in shape by self-convolution.

A detailed evolution equation for $N(d,t)$ is derived in Villermaux, Marmottant & Duplat (2004); it will be sufficient here to state that the distribution of blob sizes along the ligament at breakup $N(d,t=t_b)=N(d)$ or, alternatively, its probability density function $p_B(d)=N(d)/\int N(d)\,\mathrm{d}d$ is written as the nth-convolution

$$p_B(d)=p_1(d)^{\otimes \mathrm{n}} \tag{5.1}$$

of an elementary distribution $p_1(d)$ reflecting the distribution of sizes along the ligament just after it has detached from the liquid bulk, i.e.

$$p_1(d)=\frac{1}{\xi_b}\exp\left(-\frac{d}{\xi_b}\right). \tag{5.2}$$

The exponential shape of $p_1(d)$ is the most probable shape when only its average ξ_b is prescribed (Boltzmann distribution). It is also the distribution of intervals between random cuts of mean frequency $1/\xi_b$ along the ligament (Poisson distribution of intervals). The precise form of $p_1(d)$ is, however, of little importance as it can be shown that the final distribution $p_B(d)$ given by the evolution of $N(d,t)$ by self-convolution is attractive whatever the initial condition may be (Villermaux *et al.* 2004). This final distribution is a gamma distribution (Feller 1971)

$$p_B(x)=\frac{n^n}{\Gamma(n)}\,x^{n-1}\,\mathrm{e}^{-nx}, \tag{5.3}$$

with $x=d/\langle d\rangle$, and $\langle d\rangle=n\xi_b$. The number of convolutions is, at most, such that the final average diameter $\langle d\rangle$ restores d_0, or a fraction of d_0, and is therefore expected to be an increasing function of d_0/ξ_b in the present experiments. The detailled functional dependence is given in Villermaux *et al.* (2003).

The gamma shape closely fits the experimental distributions $p_B(d/d_0)$, with an order n which indeed increases slightly with the air velocity, as does the ratio $d_0/\xi_b\sim u_2^{1/2}$ (figure 33). This process suggests that thinner ligaments formed by faster winds produce drops which are less distributed in size (the standard deviation of the gamma distribution is $\sim 1/\sqrt{n}$).

5.2. *Droplet sizes in the spray*

The distribution of sizes from ligaments $p_B(d/d_0)$ has a universal gamma shape parameterized by the ligament initial size d_0 and the order n (figure 34*a*). However, for given operating conditions, the diameter d_0 is itself distributed although this distribution $p_L(d_0)$ is narrower than $p_B(d/d_0)$ (figure 16).

The size distribution in the spray $p(d)$ is thus the composition of the distribution of ligament size $p_L(d_0)$ and of the distribution of sizes after the breakup $p_B(d/d_0)$

$$p(d)=\int_{d_0=0}^{\infty} p_L(d_0)\,p_B\left(\frac{d}{d_0}\right)\frac{\mathrm{d}(d_0)}{d_0}. \tag{5.4}$$

This superposition is simply a convolution of the distributions in units of the logarithms of the diameters, $y=\ln(d/\langle d_0\rangle)$ and $y_0=\ln(d_0/\langle d_0\rangle)$

$$p^{\ln}(y)=\int_{y_0=-\infty}^{\infty} p_L^{\ln}(y_0)\,p_B^{\ln}(y-y_0)\,\mathrm{d}y_0. \tag{5.5}$$

It is seen in figure 35 that the convolution operation stretches the large excursion wing of $p_B(d/d_0)$ over nearly the whole range of sizes d, and recovers the size distribution in the spray $p(d)$. That distribution was found to be $p(d)\sim\exp(-nd/\langle d_0\rangle)$, with $n\simeq 3.5$ slowly increasing with the gas velocity (figure 34*b*),

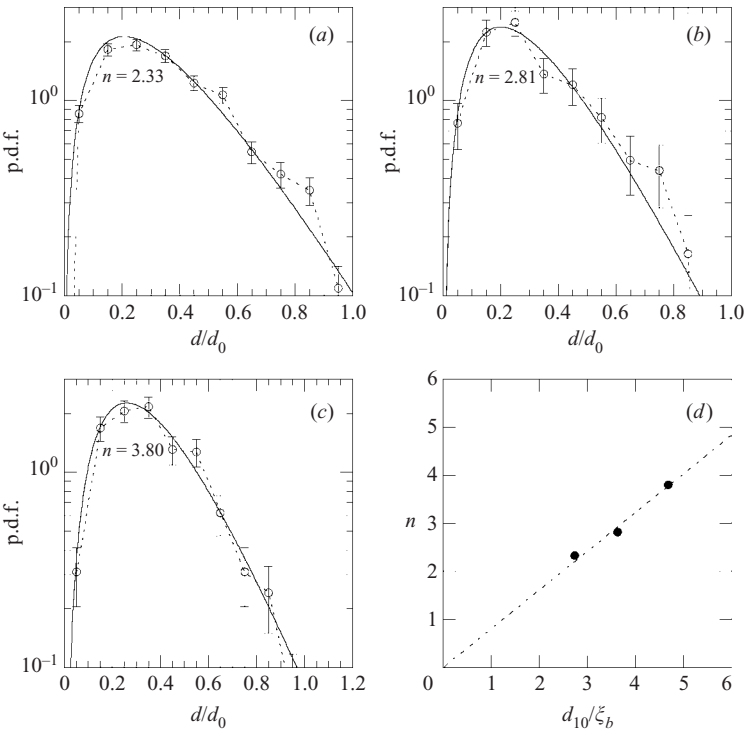

FIGURE 33. Droplet sizes distribution after ligament breakup, d_0 being the size of the ligament volume when in a sphere, (*a*) $u_2 = 29\,\mathrm{m\,s^{-1}}$; (*b*) $u_2 = 38\,\mathrm{m\,s^{-1}}$; (*c*) $u_2 = 50\,\mathrm{m\,s^{-1}}$. Lines: fit with the gamma function. (*d*) Evolution of n with the ratio of the mean droplet size to the ligament breakup thickness. Linear fit: interrupted line.

as the ratio d_0/ξ_b, see equation (3.3). The exponential shape of the global distribution, and the value of n are thus now understood as being the large sizes behaviour, and the order of the gamma distributions coming from the ligament breakup. That appears as the crucial step building-up the broad statistics in the spray.

A useful analytical illustration consists in considering a model ligament diameter distribution $p_L(d_0)$ as a uniform distribution between $d_0 = 0$ and $d_0 = s$, i.e. $p_L(d_0) = 1/s$ for $0 \leqslant d_0 \leqslant s$, then

$$p(d) \sim \int_0^\infty \left(\frac{d}{d_0}\right)^{n-1} \frac{\exp(-nd/d_0)}{sd_0} \mathrm{d}(d_0) \sim \Gamma(n-1, nd/s), \tag{5.6}$$

where $\Gamma(n-1, nd/s)$ is an incomplete gamma function whose asymptotic behaviour is $\exp(-nd/s)$ at large d/s.

6. Conclusions

The present experiments show that the atomization of a liquid volume over which blows a fast gas stream involves a succession of changes of the liquid topology, each associated with distinct instabilities.

The first instability is a shear instability of a Kelvin–Helmholtz type. It is controlled by the boundary-layer thickness δ of the gas, and produces interfacial undulations, whose selected wavelength is proportional to δ.

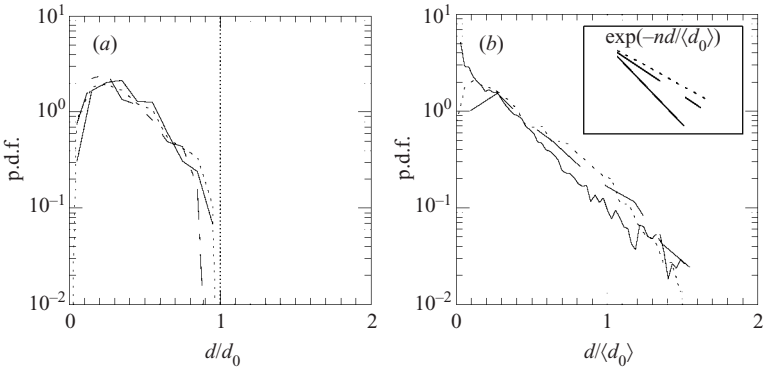

FIGURE 34. (*a*) Distribution of droplet sizes compared to the size of the ligament d_0 from which they originate, $u_2 = 27$ to $50\,\mathrm{m\,s^{-1}}$. (*b*) Distribution of droplet sizes in the spray compared to the *mean* ligament size $\langle d_0\rangle$. The slight increase of their slope with air velocity reflects the variation of the Gamma parameter n fitted on the distributions of figure 33: in the box are showed the exponential queues of the Gamma distribution.

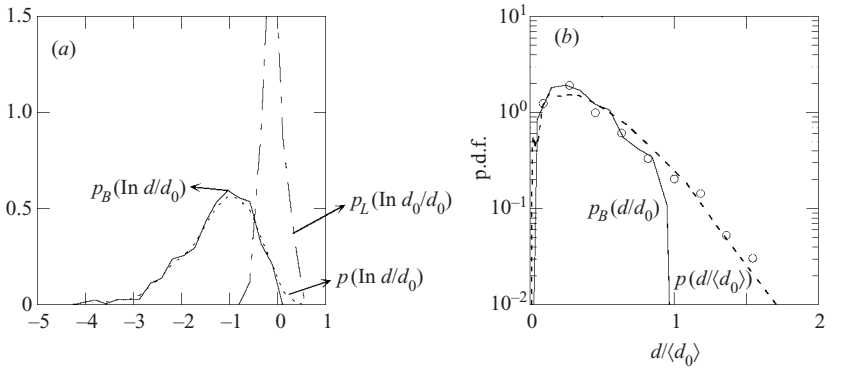

FIGURE 35. (*a*) Logarithm distributions. —, droplet sizes after breakup (p_B); - - -, ligament sizes (p_L); - - -, their convolution (p). (*b*) Linear distributions; —, p_B; - - -, convolution p; ○, experimental results at $u_1 = 0.45\,\mathrm{m\,s^{-1}}$, $u_2 = 29\,\mathrm{m\,s^{-1}}$.

When the amplitude of these undulations is large enough, the present findings suggest that these undulations undergo a transverse destabilization, of a Rayleigh–Taylor type, caused by the accelerations imposed on the liquid-gas interface by the passage of the primary undulations. These transverse corrugations have a wavelength given by $\lambda_\perp \simeq 3\delta We_\delta^{-1/3}(\rho_1/\rho_2)^{1/3}$. This last instability sets the volume of liquid which will eventually be atomized; the modulation of the crests is further amplified by the air stream forming ligaments of total volume $\lambda_\perp^3$, which ultimately break in the air stream under a capillary instability.

Although the ligament is stretched by the gas stream, the final drop size is larger than the thickness of the ligament just after it has been released from the liquid bulk, and is given, up to a proportionality factor, by $\lambda_\perp$. This is due to a coalescence mechanism between the blobs constitutive of the ligament, an aggregation process which has also its counterpart on the shape of the size distribution in the resulting spray $p(d)$, characterized by an exponential fall-off. This distribution is the composition of the relatively narrow distribution of the ligament sizes $p_L(d_0)$ and of the distribution of

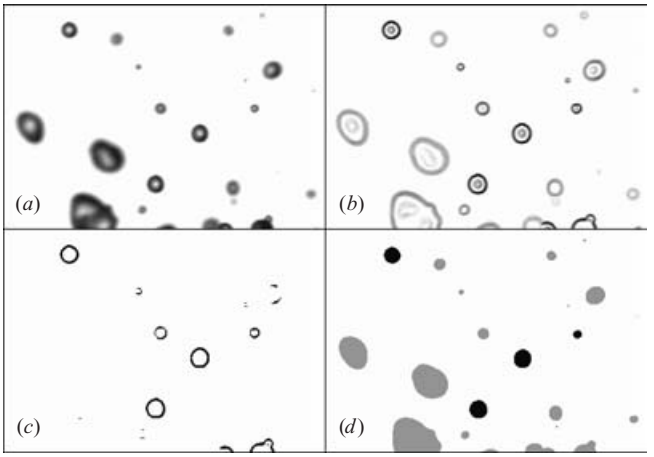

FIGURE 36. (*a*) After division by the image of the back field. (*b*) Gradient image. (*c*) Threshold on the gradient. (*d*) Surface measurements of in focus droplets.

drop sizes coming from the ligament breakup, found to be very well represented by a gamma distribution $p_B(x = d/d_0) = n^n\, x^{n-1}\, \mathrm{e}^{-nx} / \Gamma(n)$.

The exponential shape of the overall distribution $p(d) \sim \exp(-nd/\langle d_0 \rangle)$ is the large excursion behaviour of the Gamma distributions coming from the ligament breakup, a step which thus appears as a crucial one building-up the broad statistics of sprays.

Jean-Paul Barbier-Neyret designed the flash illumination system at the Laboratoire des Ecoulements Géophysiques et Industriels in Grenoble where this study first started. He is gratefully acknowledged. This work has been supported by the Société Européenne de Propulsion (SEP) under contract 910023.

Appendix A. Droplet detection algorithm

We summarize here the different steps of the droplet detection procedure on raw images of the spray (Marmottant 2001). These steps are illustrated in figure 36.

(*a*) Division by the image of the back field. This operation homogenizes the illumination behind the droplets. It uses an image of the bare back field we take prior to the recording of images with the spray. The division gives the attenuation coefficient, which is 1 when looking at a black object and 0 on the background. We preferred this method to the subtraction method because the attenuation difference is not uniform: when in front of a darker part of the screen a black object, has a smaller attenuation coefficient;

(*b*) A gradient filter is applied to enhance droplets rims. The nearer the droplet to the focal plane, the greater the gradient at its rim. The gradient is estimated by the variance of the intensity I of the 8 pixels all around a given pixel. We use the absolute value $\Sigma = \langle |\langle I - \langle I \rangle |\rangle$, where $\langle . \rangle$ is the average over the 8 neighbours. This finite difference expression provides an estimation of the modulus of a gradient that was found isotropic enough on droplets images. It was, for this reason, preferred to the classical Roberts or Sobel filters. It provides, in particular, a uniform gradient on a circular rim.

(*c*) Selection of a threshold on Σ to specify to which degree a droplet should be in focus to be detected. Since the gradient on the rim decreases with the distance to the focal plane, tuning the value of the threshold allows us to specify a depth of selection

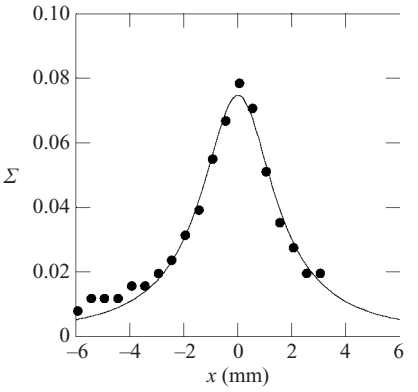

FIGURE 37. Gradient intensity on the rim as a function of defocus distance (rim of a ball bearing).

around the focal plane. This depth was calibrated experimentally with a millimetre ball bearing, displaced along the axis of view. This method provides the gradient on a rim as a function of the distance to the in-focus plane (figure 37);

(*d*) The droplets which are sufficiently in-focus all around their perimeter are selected, and their projected surface S measured on the image after division (step (*a*)). For that purpose, a threshold at half value on the grey scale was performed, which proves to give a droplet boundary that is less dependent on defocus, compared to the procedure that sets the edge at maximum gradient value (Bongiovanni, Chevaillier & Fabre 1997). The 'diameter' d of the nearly spherical droplets is defined from $S = \pi d^2/4$.

Appendix B. Turbulent conditions

The coaxial convergent injector we used in the previous experiments was designed to realize streams as laminar as possible. We will call this injector LL (laminar in the liquid and laminar in the gas).

However, in practical applications, Reynolds numbers can be as high as 10^5 with both liquid and gas streams turbulent. The impact of turbulence in a single liquid jet was studied by Mansour & Chigier (1994) and Wu & Faeth (1993), (1995). The case of turbulent coaxial jets has not received much attention except for the qualitative observations of Mayer (1994).

The issue is to determine if the break-up scenario we described is modified by the initial fluctuations due to turbulence. We have thus handled experiments using injectors with turbulence in the liquid jet and not in the gas jet, and then in both liquid and gas jets.

B.1. *Injectors*

B.1.1. *Injector TL*

Injector TL was designed to introduce turbulences in the liquid jet (turbulent liquid and laminar gas). It was realized from injector LL by the addition of obstacles (figure 38). A disk with a irregular hole of diameter 3 mm was placed in the incoming liquid to promote perturbations. A tube of diameter 10 mm with protrusions was also introduced to induce maximize initial perturbations.

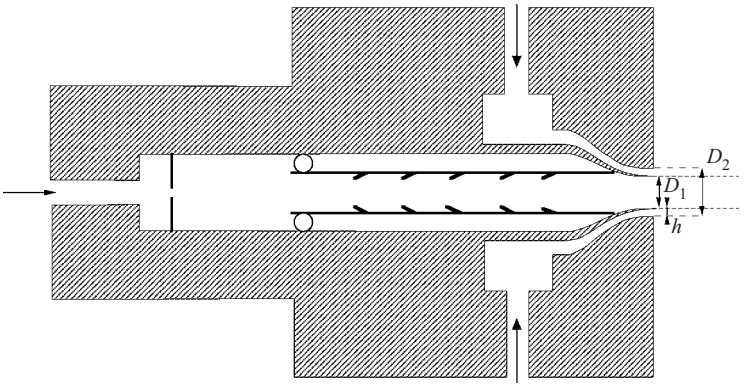

FIGURE 38. Injector TL. The exit diameter for the liquid is $D_1 = 7.6\,\text{mm}$, the annular jet of gas has an outer of diameter $D_2 = 11.4\,\text{mm}$.

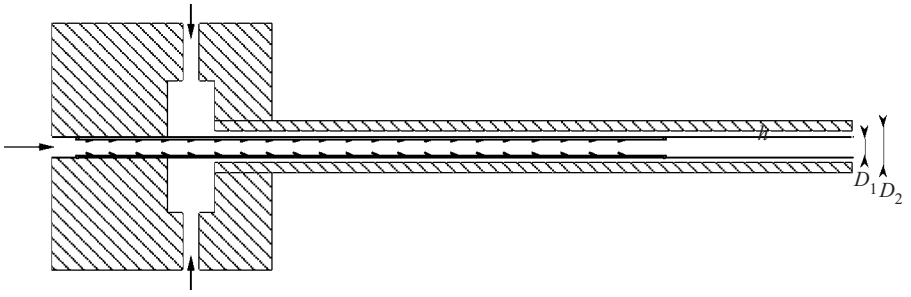

FIGURE 39. Injector TT.

B.1.2. *Injector TT*

Injector TT was designed to produce turbulences in the gas as well (turbulent liquid and turbulent gas). It is composed of two long coaxial cylinders (figure 39). Their length is 37 times the inner diameter D_1, so as to allow a fully developed turbulence to be established at exit. Protrusions in the central tube are placed to induce turbulences at the smallest velocities. The exit diameters are the same as with the convergent injector LL or its TL version.

The turbulence intensity in the central jet was characterized by anemometry at the tube exits (figure 40). The turbulence intensity u_{rms}/u is about 8% at the centre, and reaches 17% at the boundary of the central jet for $Re = 10^4$, which is consistent with known measurements in tubes (Schlichting 1987).

The boundary-layer thickness in the annular gas jet can be determined from the air velocity profiles across the gap between the inner and outer exits (figure 41*a*), as with the laminar flow injector. The most convenient way to estimate the thickness of the boundary layer is to measure the vorticity thickness, $\delta = u_{\max}/(\mathrm{d}u/\mathrm{d}y)|_{max}$, ratio of the maximum velocity at the centre and of the maximum velocity gradient (figure 41*b*). For small Reynolds numbers the vorticity thickness appears to be constant. The flow then approaches a Poiseuille flow, of parabolic profile $u(y) = u_{max}\,4y(h - y)/e^2$. Indeed, the annulus gap is long enough to allow the development of such a profile (the tube length is 140 gap width when the Poiseuille development length $\approx 0.035\,hRe_2$ is about $35h$ at $Re_2 = 1000$). The velocity gradient at the edge is $(\mathrm{d}u/\mathrm{d}y)|_{y=0} = 4u_{\max}/h$, and thus proportional to maximum velocity,

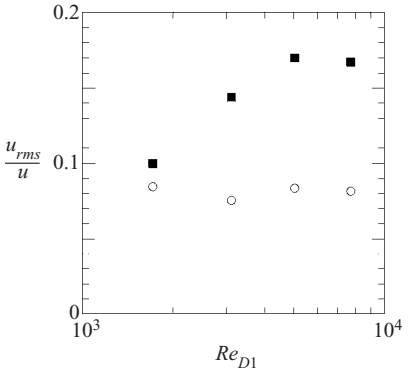

FIGURE 40. Turbulence intensity in the central jet of injector TT; ○, at the centre of the jet, ■, at boundary of the jet.

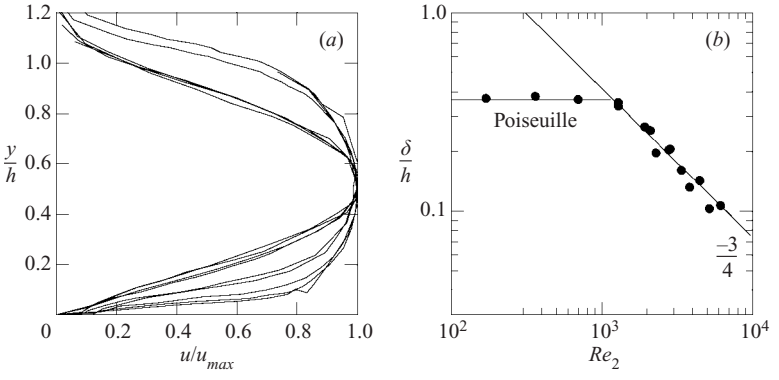

FIGURE 41. (*a*) Air profile in the gas across the exit crown of injector TT, with u_{max} increasing from 1.5 m s^{-1} to 54.5 m s^{-1}. (*b*) Boundary-layer thickness δ in the air on the wall that separates air from liquid as a function of $Re_2 = u_{\max} h/\nu_2$. Interpolation of δ by $0.35\,h$ for small Reynolds numbers, and by $74\,Re_2^{-3/4}$ for large Reynolds numbers.

which gives a constant vorticity thickness of $\delta = h/4$, close to experimental findings for $Re_2 < 1000$.

For $Re_2 > 1000$, the flow is turbulent in the channel and the friction velocity at the wall u_τ, defined by $\rho_2 u_\tau^2 = \mu_2 (\mathrm{d}u/\mathrm{d}y)|_{y=0}$ is, according to Blasius (Schlichting 1987)

$$\frac{u_\tau}{u_2} = \frac{0.164}{Re_2^{1/8}}, \tag{B 1}$$

giving a boundary-layer thickness δ which scales as

$$\frac{\delta}{h} = \frac{37.2}{Re_2^{3/4}}, \tag{B 2}$$

a trend consistent with our measurements with, however, a different prefactor of 74.

B.2. *Wavelength of the primary instability*

Figure 42 shows that, with no air flow, the disturbances at the liquid surface are alike with injectors TL and TT, whereas the injector LL does not disturb liquid surfaces up to $Re_1 = 19\,000$.

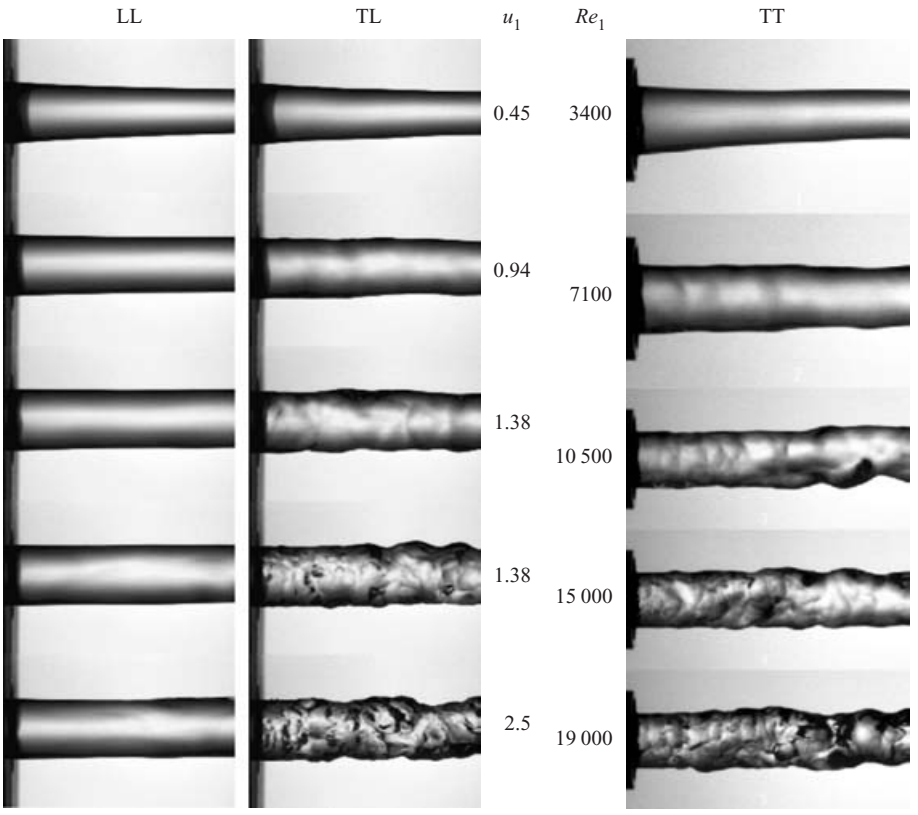

FIGURE 42. Surface profile with injectors LL (laminar in liquid and in gas), TL (turbulent liquid, laminar gas) and TT (turbulent in liquid and in gas) as a function of liquid Reynolds number $Re_1 = u_1 D_1/\nu_1$, with no air flow.

With the air stream, the measurement of the wavelength separating successive axisymmetric crests was performed on a water jet of $2\,\mathrm{m\,s^{-1}}$, varying $Re_2 = hu_2/\nu_2$. With the turbulent air flow of injector TT, the wavelength λ was proportional to $Re_2^{-3/4}$, and thus the ratio λ/δ was found to be constant. With injectors TL and LL, the wavelength is proportional to $Re_2^{-1/2}$, and the ratio λ/δ is of the same order (figure 43).

The presence of turbulent disturbances in the liquid or in the gas thus does not modify the selection of the primary wavelength, which is, in law, and in absolute value, prescribed by δ, whether this lengthscale is ruled by laminar or turbulent scalings. This is a direct consequence of the large momentum ratio $M = \rho_2 u_2^2/\rho_1 u_1^2$ between the streams (see Villermaux 1998*a*, *b* for a discussion on that point). Indeed, the pressure scale responsible for the corrugations of the liquid interface from the liquid turbulent motions is $\rho_1 u_{rms}^2$ when the pressure scale responsible for the amplication of the primary disturbaces is $\rho_2 u_2^2$. When $M > 1$, and with $u_{rms} \approx 0.08 u_1$, it is clear that $\rho_2 u_2^2 \gg \rho_1 u_{rms}^2$; the liquid, whether it be turbulent or not, is destabilized in a passive way.

B.3. *Droplet sizes in the spray*

The drops formed in the spray by the turbulent injector are characterized by the very same phenomenology as those formed by a laminar injector. The size distribution

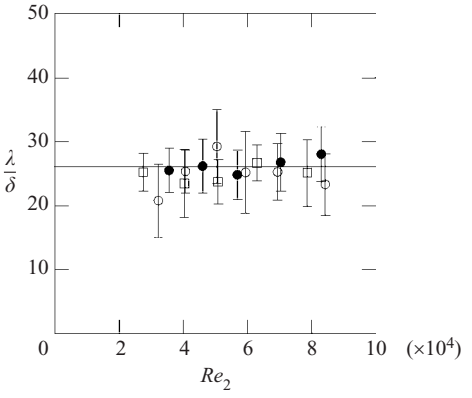

FIGURE 43. Wavelength to air boundary layer ratio at $u_1 = 2\,\mathrm{m\,s^{-1}}$; ○, injector LL; □, injector TL; ●, injector TT.

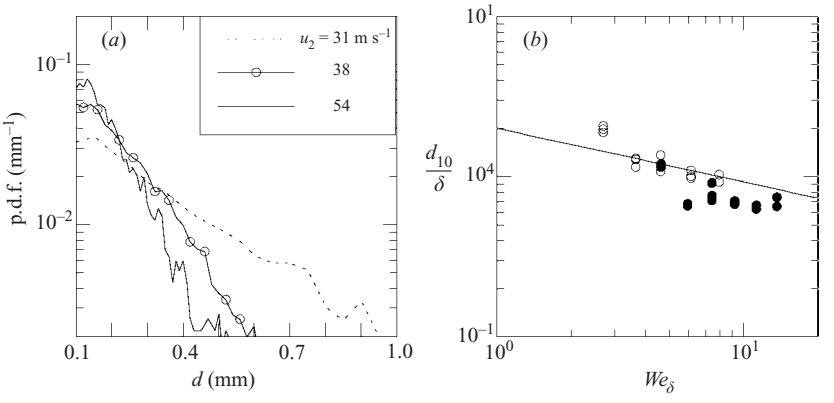

FIGURE 44. (*a*) Distribution of droplet sizes issuing from the turbulent injector TT. (*b*) Mean diameter of droplets in the spray at $u_1 = 2\,\mathrm{m\,s^{-1}}$, ○, injector LL; ●, injector TT.

exhibits the same exponential decay, and, as the gas stream velocity is increased, the mean drop size, when normalized by the proper lengthscale δ setting the primary instability wavelength, follows the same trend (figure 44). The mean drop size is somewhat smaller, a small effect probably due to an incomplete convolution sequence for restoring $\langle d_0 \rangle$.

In conclusion, turbulent fluctuations superimposed on both the liquid and the gas streams do not modify the atomization process, from the initial primary destabilization to the droplet size.

REFERENCES

ANDREAS, E. L., PATTISON, M. & BELCHER, S. E. 2001 Production rates of sea-spray droplets: clarification and elaboration. *J. Geophys. Res.* **106** (C4), 7157–7161.

ANGUELOVA, M. & BARBER, R. P. 1999 Spume drops produced by the wind tearing of wave crests. *J. Phys. Oceanogr.* **29**, 1156–1165.

BAYVEL, L. & ORZECHOWSKI, Z. 1993 *Liquid Atomization.* Taylor & Francis.

BERNAL, L. & ROSHKO, A. 1986 Streamwise vortex structure in plane mixing layers. *J. Fluid Mech.* **170**, 499–525.

Betchov, R. & Szewczyk, A. 1963 Stability of a shear layer between parallel streams. *Phys. Fluids* **6**, 1391–1396.

Bongiovanni, C., Chevaillier, J. P. & Fabre, J. 1997 Sizing of bubbles by incoherent imaging: defocus bias. *Exps. Fluids* **23**, 209–216.

Chandrasekhar, S. 1961 *Hydrodynamic and Hydromagnetic Stability*. Dover.

Cohen, R. D. 1990 Steady-state cluster size distribution in stirred suspensions. *J. Chem. Soc. Faraday Trans.* **86**, 2133–2138.

Cohen, R. D. 1991 Shattering of a liquid drop due to impact. *Proc. R. Soc. Lond.* A **435**, 483–503.

Dimotakis, P. 1986 Two-dimensional shear layer entrainment. *AIAA J.* **24**, 1791–1796.

Eggers, J. 1997 Nonlinear dynamics and breakup of free-surface flows. *Rev. Mod. Phys.* **69**, 865–929.

Eroglu, H. & Chigier, N. 1991 Wave characteristics of liquid jets from airblast coaxial atomizers. *Atom. Sprays* **1**, 349–366.

Faragó, Z. & Chigier, N. 1992 Morphological classification of disintegration of round liquid jets in a coaxial air stream. *Atom. Sprays* **2**, 137–153.

Feller, W. 1971 *An Introduction to Probability Theory and its Applications.* Wiley.

Frankel, I. & Weihs, D. 1985 Stability of a capillary jet with linearly increasing axial velocity (with application to shaped charges). *J. Fluid Mech.* **155**, 289–307.

Gaster, M. 1962 A note on the relation between temporally-increasing and spatially-increasing disturbances in hydrodynamic stability. *J. Fluid Mech.* **14**, 222–224.

Hanson, A. R., Domich, E. G. & Adams, H. S. 1963 Shock tube investigation of the break-up of drops by air blasts. *Phys. Fluids* **6**, 1070–1080.

Hinze, J. O. 1949 Critical speeds and sizes of liquid globules. *Appl. Sci. Res.* **A1**, 273–288.

Hinze, J. O. 1955 Fundamental of the hydrodynamic mechanism of splitting in dispersion processes. *AIChE* **1-3**, 289–295.

Hoyt, J. W. & Taylor, J. 1977 Waves on water jet. *J. Fluid Mech.* **83**, 119.

Huerre, P. & Rossi, M. 1998 In *Hydrodynamics and Nonlinear Instabilities* (ed. C. Godrche & P. Manneville), pp. 81–386. Aléa Saclay.

Joseph, D. D., Belanger, J. & Beavers, G. 1999 Breakup of a liquid drop suddenly exposed to a high-speed airsteam. *Intl J. Multiphase Flow* **25**, 1263–1303.

Kolmogorov, A. N. 1949 On the breakage of drops in a turbulent flow (in Russian). *Dokl. Akad. Nauk SSSR* **66**, 825–828.

Krzeczkowski, S. A. 1980 Measurement of liquid droplet mechanism. *Intl J. Multiphase Flow* **6**, 227–239.

Lane, W. 1951 Shatter of drops in streams of air. *Indust. Engng Chem.* **43**, 1312–1317.

Lasheras, J. & Hopfinger, E. 2000 Liquid jet instability and atomization in a coaxial gas stream. *Annu. Rev. Fluid Mech.* **32**, 275–308.

Lasheras, J., Villermaux, E. & Hopfinger, E. 1998 Breakup and atomization of a round water jet by a high-speed annular jet. *J. Fluid Mech.* **357**, 351–379.

Lefebvre, A. H. 1989 *Atom and Sprays.* Hemisphere.

Lewis, D. J. 1950 The instability of liquid surfaces when accelerated in a direction perpendicular to their planes ii. *Proc. R. Soc. Lond.* A **202**, 81–96.

Longuet-Higgins, M. S. 1992 The crushing of air cavities in a liquid. *Proc. R. Soc. Lond.* A **439**, 611–626.

Mansour, A. & Chigier, N. 1994 Turbulence characteristics in cylindrical liquid jets. *Phys. Fluids* **6**, 3380–3391.

Marmottant, P. 2001 Atomisation d'un courant liquide dans un courant gazeux. PhD thesis, Institut National Polytechnique de Grenoble.

Marmottant, P. & Villermaux, E. 2004 Fragmentation of stretched liquid ligaments. *Phys. Fluids* (to appear).

Mayer, W. 1994 Coaxial atomization of a round liquid jet in a high speed gas stream: a phenomenological study. *Exps. Fluids* **16**, 401–410.

Meier, G., Klöpper, A. & Grabitz, G. 1992 The influence of kinematic waves on jet break down. *Exps. Fluids* **12**, 173–180.

Novikov, E. A. & Dommermuth, D. G. 1997 Distribution of droplets in a turbulent spray. *Phys. Rev.* E **56**, 5479–5482.

Pilch, M. & Erdman, C. 1987 Use of breakup time data and velocity history data to predict the maximum size of stable fragments for acceleration-induced breakup of a liquid drop. *Intl J. Multiphase Flow* **13**, 741–757.

Plateau, J. 1873 *Statique expérimentale et théorique des liquides soumis aux seules forces moléculaires.* Gauthier Villars, Paris.

Ranger, A. & Nicholls, J. 1969 Aerodynamic shattering of liquid drops. *AIAA J.* **7**, 285–290.

Rayleigh, Lord 1879 On the stability of jets. *Proc. Lond. Math. Soc.* **10**, 4.

Rayleigh, Lord 1880 On the stability, or instability of certain fluid motion. *Proc. Lond. Math. Soc.* **11**, 57.

Rayleigh, Lord 1883 Investigation of the character of the equilibrium of an incompressible heavy fluid of variable density. *Proc. R. Soc.* **14**, 170–177.

Raynal, L. 1997 Instabilité et entraînement à l'interface d'une couche de mélange liquide–gaz. PhD thesis, Université Joseph Fourier, Grenoble.

Raynal, L., Villermaux, E., Lasheras, J. & Hopfinger, E. 1997 Primary instability in liquid gas shear layers. In *11th Symp. on Turbulent Shear Flows*, , vol. 3, pp. 27.1–27.5.

Schlichting, H. 1987 *Boundary layer theory*, 7th edn. McGraw-Hill.

Simmons, H. 1977*a* The correlation of drop-sizes distributions in fuel nozzles sprays. Part i. *J. Engng Power* **7**, 309–314.

Simmons, H. 1977*b* The correlation of drop-sizes distributions in fuel nozzles sprays. Part ii. *J. Engng Power* **7**, 315–319.

Taylor, G. I. 1950 The instability of liquid surfaces when accelerated in a direction perpendicular to their planes i. *Proc. R. Soc. Lond.* A **201**, 192–196.

Thoroddsen, S. & Takehara, K. 2000 The coalescence cascade of a drop. *Phys. Fluids* **12**, 1265–1267.

Villermaux, E. 1993 Auto-oscillation et mélange dans les écoulements recirculants. PhD thesis, Paris VI.

Villermaux, E. 1998*a* Mixing and spray formation in coaxial jets. *J. Prop. Power* **14**, 807–817.

Villermaux, E. 1998*b* On the role of viscosity in shear instabilities. *Phys. Fluids* **10**, 368–373.

Villermaux, E. & Clanet, C. 2002 Life of a flapping liquid sheet. *J. Fluid Mech.* **462**, 341–363.

Villermaux, E., Marmottant, P. & Duplat, J. 2004 Ligament mediated spray formation. *Phys. Rev. Lett.* (to appear).

Weber, C. 1931 Zum Zerfall eines Flüssigkeitsstrahles. *Z. Angew. Math. Mech.* **2**, 136.

Wu, P.-K. & Faeth, G. 1993 Aerodynamic effects on primary breakup of turbulent liquids. *Atom. Sprays* **3**, 265–289.

Wu, P.-K. & Faeth, G. 1995 Onset and end drop formation along the surface of turbulent jets in still gases. *Phys. Fluids* **7**, 2915–2917.

Wu, P.-K., Ruff, G. & Faeth, G. 1991 Primary break-up in liquid–gas mixing layers. *Atom. Sprays* **1**, 421–440.

Yatsuyanagi, N., Sakamoto, H. & Sato, K. 1994 Atomization characteristics of liquid jets injected into a high-velocity flow field. *Atom. Sprays* **4**, 451–471.

Zaleski, S., Li, J., Scardovelli, R. & Zanetti, G. 1996 Direct simulation of multiphase flows with density variations. In *Colloque IUTAM on Variable Density Low Speed Turbulent Flows, Marseille 8–10 Juillet 1996* (ed. L. Fulachier & F. Anselmet). Kluwer.